Molecular Dynamics Simulation of Nanoporous Graphene for Selective Gas Separation

by

Harold Au

B.S., Engineering, Duke University (2011)

Submitted to the Department of Mechanical Engineering
in partial fulfillment of the requirements for the degree of

Master of Science in Mechanical Engineering

at the

MASSACHUSETTS INSTITUTE OF TECHNOLOGY

September 2012

Author .....
Department of Mechanical Engineering
August 10, 2012

Certified by ....
Nicolas G. Hadjiconstantinou
Professor
Thesis Supervisor

Certified by .....
Rohit Karnik
Associate Professor
Thesis Supervisor

Accepted by ....
David E. Hardt
Graduate Officer, Professor of Mechanical Engineering

Molecular Dynamics Simulation of Nanoporous Graphene for Selective Gas Separation

by

Harold Au

Submitted to the Department of Mechanical Engineering
on August 10, 2012, in partial fulfillment of the
requirements for the degree of
Master of Science in Mechanical Engineering

Abstract

Graphene with sub-nanometer sized pores has the potential to act as a filter for gas separation with considerable efficiency gains compared to traditional technologies. Nanoporous graphene membranes are expected to yield high selectivity through molecular size exclusion effects, while achieving high permeability due to the very small thickness of graphene.

In this thesis, we model the separation of gas components from a mixture using a graphene sheet with engineered pores of different sizes. We employ molecular dynamics simulations to calculate a large number of molecular trajectories, and thus obtain low-statistical-uncertainty estimates of transport rates through the membrane. Simulations are performed on two different gas mixtures - a helium-sulfur hexafluoride mixture, for which the large difference in molecular size lends itself to a size-based separation approach, and a hydrogen-methane mixture, which is relevant to natural gas processing. Our simulations show that graphene membranes with large pores are permeable to both gases in the mixture. As pore sizes are reduced, we observe a greater decrease in the permeability of the larger species that results in a molecular size exclusion effect for a range of pore sizes that are still permeable to the smaller species. This indicates that a pore size can be determined that achieves high selectivity in gas separation, while exhibiting high permeability for the desired gas species.

We expect this work to form the basis for the design of an energy-efficient graphene-based gas separation device. The simulation-based approach described here can be very useful for guiding experimental efforts which are currently limited by the difficulty associated with creating pores of a specific size in otherwise pristine graphene.

Thesis Supervisor: Nicolas G. Hadjiconstantinou
Title: Professor

Thesis Supervisor: Rohit Karnik
Title: Associate Professor

Acknowledgments

First and foremost, I would like to thank my advisor Professor Nicolas Hadjiconstantinou for his patient support, invaluable guidance and good humor. He has given me the courage to delve into a new field and reap its many rewards. My gratitude also goes out to my co-advisor Professor Rohit Karnik for his direction throughout the course of this thesis, and for inspiring me with his wealth of ideas.

I am indebted to Visiting Professor Pietro Poesio from the University of Brescia for contributing to the code used in this thesis. His enthusiasm for the new subject of molecular dynamics was infectious.

Colin Landon has been immensely helpful since the day I joined the group, with his timely technical advice and the many hours he dedicated to ensure that my simulations ran smoothly. Michael Boutilier was a brilliant partner-in-crime, and I thoroughly enjoyed collaborating with him on this entire undertaking. Without his untiring help, this project would not have been as smooth-sailing. I am also grateful to the other members of my research group, Jean-Philippe Peraud, Toby Klein and Kostantinos Kleovoulou for their advice and friendship, and to my collaborators David Cohen-Tanugi and Greta Gronau for their technical advice on LAMMPS.

My like-minded friends from Mechanical Engineering, Sin-Cheng Siah, Mei Yi Cheung and Ronald Chan have filled my life with joy, and alternatively, encouragement. I will always cherish their friendship.

I am grateful to Singapore Technologies Engineering Ltd for its financial support.

Special thanks to my parents Winston and Michelle, for their unwavering faith, encouragement and love. You have shown me the meaning of love and sacrifice.

To my best friend and soulmate Sera, thank you! You have been a pillar of strength all these years, and the past two months have been beautiful with you by my side.

Contents

List of Figures

List of Tables

Chapter 1

Introduction

Industrial gas separation relies on three major processes - pressure swing adsorption (PSA), cryogenic distillation and membrane gas separation. PSA technology is used to separate a target gas species from a mixture of gases under pressure, according to the species' molecular characteristics and affinity for an adsorbent material. Special adsorptive materials such as zeolites are used as molecular sieves, preferentially adsorbing the target gas species at high pressure. The process then swings to low pressure to desorb the adsorbent material. The PSA process is, by far, the most extensively used industrial process to separate H_2 from a mixture of gases [3]. However, industrial applications often require PSA gas purification processes to be operated at high temperatures, which decreases the sorbent selectivity for the desired species and reduces the performance of the gas purification process. Hence, significantly lower flow rates are used, in order to achieve a high performance [4].

Cryogenic distillation separates the target gas species from a mixture of gases at low temperatures based on the difference in boiling temperatures of the gas components [5]. However, cryogenic distillation requires a phase change, and thus consumes a considerable amount of energy [3, 6, 7].

Other than PSA and cryogenic separation, membrane separation techniques have attracted the widest interest. Membranes are barriers that only allow selected materials to permeate across them. Membrane separation processes offer several advantages over the more mature and commercially-available PSA and cryogenic separation pro-

cesses [3].

1.1 Membrane Gas Separation

1.1.1 Mechanisms

Membrane gas separation is a pressure-driven process that can be attributed to four mechanisms: (i) Knudsen diffusion, (ii) molecular sieving, (iii) solution-diffusion, and (iv) surface diffusion [3, 8, 9]. In some cases, gas molecules can pass through the membrane by more than one mechanism.

Knudsen diffusion occurs when the relevant physical length scale in a porous membrane - in this case the pore diameter, L, is smaller than the mean free path for the gas being separated, λ, that is, when the Knudsen number, $Kn = \frac{\lambda}{L}$, is large. In this regime, the permeability of each species scales with its Knudsen diffusivity which depends on the square root of its molar mass [10]. As a result, the selectivity of this process is somewhat limited.

If pore sizes become sufficiently small, molecular sieving can be used to separate molecules that differ in kinetic diameter [8]. Only the smaller gas molecules can permeate through the membrane. In other words, separations based on molecular sieving operate on a molecular size exclusion principle [3].

The solution-diffusion mechanism is the most commonly used physical model to describe gas transport through dense membranes [8]. A gas molecule is adsorbed on one side of the membrane, dissolves in the membrane material, diffuses through the membrane and desorbs on the other side of the membrane. Hence, solution-diffusion separations are based on both solubility and mobility of one species in a solid effective barrier [9].

Surface diffusion can occur in parallel with Knudsen diffusion [3, 8]. Gas molecules are adsorbed on the pore walls of the membrane and migrate along the surface. Surface diffusion increases the permeability of the gas components that are more strongly adsorbed on the membrane pores. At the same time, the effective pore diameter is

reduced when adsorbed gas molecules occlude the pores. As a result, transport of non-adsorbing components is reduced and selectivity is increased [8]. However, the positive contribution of surface diffusion only works for certain temperature ranges and pore diameters.

1.1.2 Classifications

Membrane materials and structures are highly tailored for specific gas separation applications, in order to achieve high membrane permeability, selectivity and robustness. Permeability is the rate at which a compound permeates through a membrane, and is typically used to provide an indication of the capacity of a membrane; a high permeability means a high throughput [11]. Permeability is inversely proportional to membrane thickness. Hence, most commercial membranes consist of thin (about 0.1 to 5 μm) selective layers on porous support layers that provide mechanical strength [12, 13]. Selectivity is the ability of a membrane to accomplish a given separation, and is dependent on the relative permeability of the membrane for the gas species [14]. The economic viability of a membrane depends on its throughput, selectivity, cost and durability. A high throughput alone would not be useful unless the membrane selectivity exceeds an acceptable level. On the other hand, a membrane with a high selectivity and low throughput may require such a large membrane surface area that it becomes economically unattractive [11] or structurally unfeasible.

Commercial membrane gas separation modules generally employ organic polymers such as polydimethylsiloxane (PDMS) and polycarbonates as nonporous membranes based on the solution-diffusion transport mechanism [14]. However, polymeric membranes show high selectivities and low throughput when compared to porous materials. Robeson [1] has demonstrated that polymeric membranes generally undergo a tradeoff limitation between permeability and selectivity, as illustrated in the characteristic selectivity/permeability diagram of H_2/CH_4 separation (Figure 1-1). As membrane selectivity increases, permeability decreases and vice versa, and an upper bound exists in Figure 1-1. Unless significant advancement in solubility selectivity can be achieved, the upper bound would represent the asymptotic endpoint in the perfor-

mance of polymeric membranes whose separation properties are related to solution-diffusion transport mechanisms [14]. Hence, significant industrial efforts have been focused on developing porous inorganic membranes such as zeolites, as well as carbon-based molecular sieves, which can be used to achieve higher selectivity/permeability combinations. Carbon membranes are believed to contain slit-shaped pores. The pore size determines the degree of interaction between molecules and pores, which affects the separation mechanism in these membranes. Molecular sieving is dominant when effective pore diameters are on the molecular scale (3-5 Å) [14], improving membrane selectivity.

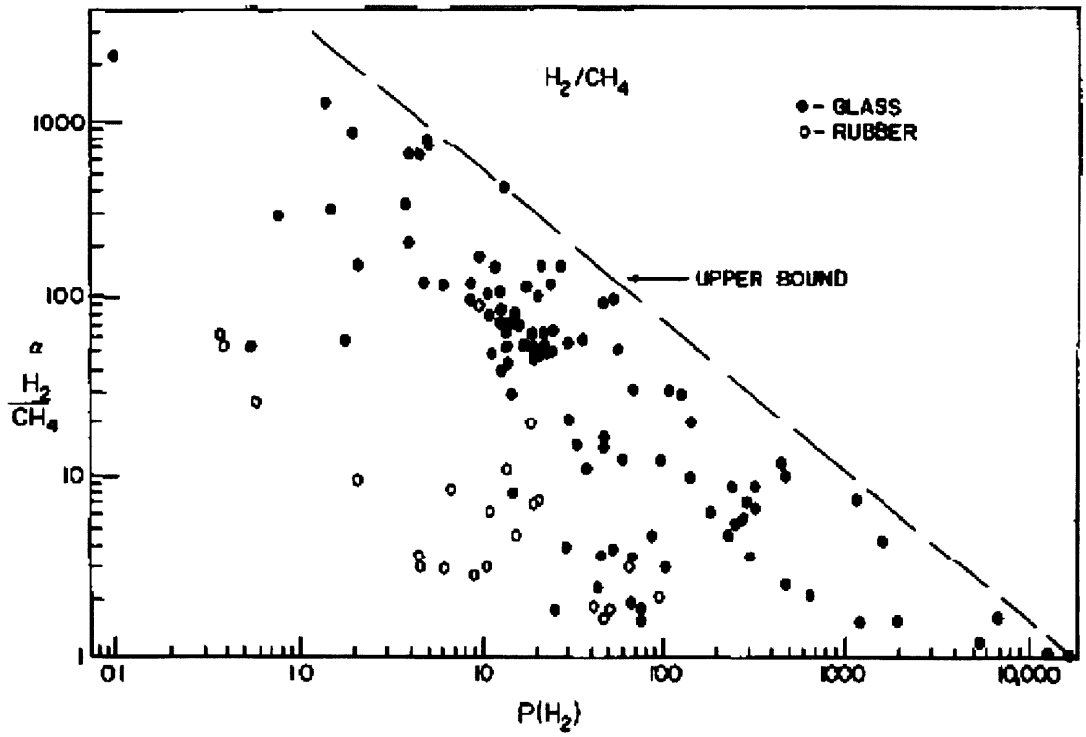

Figure 1-1: Robeson plot for H_2/CH_4 separation [1]. H_2/CH_4 selectivity is plotted against H_2 permeability. Data points represent individual polymers. The presence of an upper bound indicates a tradeoff limitation between permeability and selectivity.

1.1.3 Advantages and Applications

Membrane separation systems offer several benefits over other separation approaches, especially for small-to-medium scale applications [12]. They rely on a pressure-driven process that employs no moving parts and requires no exotic chemicals, and are thus suitable for use in remote locations where reliability is critical [14]. Membrane separation systems exhibit low energy requirements as compared to cryogenic distillation as they do not require a phase change, and possess a high degree of flexibility in their possible configurations in industrial plants [15].

These attributes are very important in the context of pressing environmental and energy-related applications [16], such as natural gas processing [12, 16], CO_2/N_2 separation for carbon dioxide sequestration, CO_2/H_2 for syngas production and O_2/air separation for oxycombustion [15]. Natural gas processing is the largest industrial gas separation application, and in the last 10 years, the total worldwide market for new natural gas separation equipment was estimated at \$ 5 billion per year [17]. Membrane-based removal of natural gas contaminants is the most rapidly growing segment of the membrane gas separation industry, especially in applications for the separation of carbon dioxide, nitrogen, and heavy hydrocarbons [17]. However, current industrial applications of membrane gas separation represent only a small fraction of the potential applications in refineries and chemical industries [14], especially in light of the development of novel materials for gas separation.

1.2 Promise of Nanoporous Graphene Membranes

Graphene, an atomically thin single sheet of graphite comprising sp^2-bonded carbon atoms arranged in a hexagonal lattice [18, 19], holds significant promise for gas separation due to its unique properties. It exhibits remarkable mechanical properties, including an intrinsic failure strength of 130 GPa [20]. It is stable in air, and can resist oxidation at temperatures up to 500 °C [21]. Pristine graphene has been shown to be impermeable to gases [22]. However, several studies have suggested that graphene has the potential to induce highly selective transport by generation of pore defects

[23, 24, 25, 26, 27, 28], in which atoms can be removed from the graphene lattice to create pores of a specific size and geometry. Very high membrane selectivity may be achieved through molecular size exclusion effects, whereby smaller gas species pass through the pores while larger gas species are blocked. Also, high permeability is expected as the atomic thickness of graphene provides little resistance to flow across the pores.

Nanoporous graphene opens up a new frontier in the field of gas separation because its very small thickness allows for a very high permeance and thus very high energy efficiency, while also maintaining high selectivity through steric effects at the entrance of the angstrom-sized pores. This represents a significant improvement over traditional polymer membranes, which are limited by the fundamental permeability/selectivity tradeoff illustrated in the Robeson diagrams [1]. In fact, computational studies have predicted that gas permeance through nanoporous graphene is about 3 orders of magnitude larger than that in existing membranes, while achieving excellent selectivity in the range 10^8 to 10^{23} for H_2/CH_4 [24].

Although nanoporous graphene membranes have yet to be created for gas separation, considerable progress has been made in the field of graphene synthesis. Within six years of its discovery in 2004 [29], single or few-layer graphene sheets on large areas have been synthesized [18, 30, 31], and 30-inch sheets have been transferred on a roll-to-roll basis [32]. This suggests the feasibility of commercial production, and may enable the future design of a graphene-based gas separation device to be realized.

1.3 Prior Simulation Work

The key challenge facing the design of a graphene-based gas separation device is the difficulty of experimentally generating sub-nanometer pores with precisely-controlled sizes that are required for molecular size exclusion. Several methods have been proposed for generating pore defects, including oxidation [33], ion bombardment [34, 35, 36, 37, 38] and electron-beam irradiation [39, 40], but measurements of gas transport rates through nanoporous graphene membranes have yet to be reported.

Hence, molecular simulations can be very helpful in elucidating the effect of pore size on gas transport across nanoporous graphene membranes.

Prior molecular simulation work [23, 24, 26] has largely focused on quantum mechanics-based approaches, which determine the electronic structures of atoms in order to understand intermolecular interactions. Jiang et al. performed first principles Density Functional Theory (DFT) calculations to argue that nanoporous graphene has the potential to become the "ultimate" membrane for gas separation. The potential energy surface and dynamics of H_2 and CH_4 molecules passing through subnanometer pores created in a graphene sheet was modeled using both the Perdew, Burke, and Ernzerhof (PBE) [41] functional form of the generalized-gradient approximation (GGA) and the Rutgers-Chalmers van der Waals density functional (vdW-DF) [42, 43] for exchange and correlation [24], the latter of which accounts for dispersion interactions. The PBE method was then incorporated into quantum mechanics-based First Principles Molecular Dynamics (FPMD) simulations, which showed that by suitably tuning nanopore sizes to achieve filtration by size exclusion, graphene can provide selectivities on the order of 10^8 to 10^{23} for H_2/CH_4 while exhibiting a H_2 permeance of 1 $\mathrm{mol/m^2\,s\,Pa}$. This is up to 5 orders of magnitude larger than traditional polymeric membranes [12, 44], making it questionable, since it is significantly larger than the equilibrium molecular flux of dilute H_2 on a membrane (0.2 $\mathrm{mol/m^2\,s\,Pa}$); this discrepancy is even greater for other molecular species.

This illustrates a key limitation of DFT, and quantum-based approaches in general — although these calculations are invaluable for studying the energetics of atomic interactions, they are currently too computationally intensive to study gas transport in devices. In the study by Jiang et al. [24], only 15 gas molecules were simulated, of which 4 crossings were observed and used to calculate the permeance. These numbers are very small and most possibly insufficient to predict transport properties; it is therefore not surprising that their result is questionable. Even though previous simulations [45] have shown that surface adsorption followed by diffusion to the pore contributes to the flux through the pore, this was found to be small at the temperatures of interest here. At the temperatures of interest, gas molecules have high

enough kinetic energy to directly overcome the energy barrier at the pore mouth, hence surface adsorption and diffusion processes are less important.

Schrier [26] performed highly computationally-intensive MP2 simulations using cc-pVTZ basis sets to model the potential energy surface of He atoms passing through subnanometer pores created in a graphene sheet, and investigate the role of quantum and transmission effects as a function of temperature. At very low temperatures, classical transmission is exceedingly unlikely since there are very few atoms in the high energy tail of the Boltzmann distribution, while quantum tunneling processes are orders of magnitude more likely to occur. However, at 300 K, quantum effects account for only a 16 % increase in the transmission of ^{4}He, and the enhancement further decreases at higher temperatures [26]. This result provides justification for neglecting quantum effects and employing classical Molecular Dynamics (MD) simulations for investigating gas transport across nanoporous graphene membranes (at room temperature).

1.4 Scope of Work

The challenges associated with realizing nanoporous graphene membranes for gas separation necessitates a theoretical, molecular simulation-based study to elucidate the effect of pore size on gas transport. The objective of this thesis is to calculate the transport of different gas species across a graphene sheet with engineered pore sizes using MD simulation techniques, in order to demonstrate that a pore size can be determined that achieves high selectivity and permeability of the desired species.

The computational efficiency afforded by MD simulations over quantum mechanics-based approaches will enable the simulation of a larger number of molecular trajectories over a longer timescale, allowing low-statistical-uncertainty estimates of transport rates through a graphene membrane to be obtained. Although there are numerous permutations of gases that are relevant to industrial gas separation, this thesis will focus on the separation of: (1) hydrogen from methane, and (2) helium from sulfur hexafluoride. The difference in the sizes of H_2 versus CH_4, and He versus SF_6 makes

them amenable for this initial proof-of-concept study, while simulations on the latter mixture will further serve to guide preliminary experimental work on the gases. In addition, the separation of H_2 from CH_4 has much industrial significance. It is one of the major requirements before the distribution of natural gas [12], and will become increasingly important as the world moves towards a hydrogen economy, in which existing natural gas infrastructure can be used for economical hydrogen distribution [46].

Chapter 2 reviews the numerical features of the MD simulation algorithm and the force fields employed. Chapter 3 presents a model of gas separation using a nanoporous graphene sheet, while Chapter 4 describes the simulation parameters in detail, in the context of numerical implementation in LAMMPS. Chapter 5 discusses the separation of H_2 from CH_4 and He from SF_6, and demonstrates that a pore size can be determined that achieves high selectivity and permeability for the desired gas species.

Chapter 2

Molecular Dynamics (MD)

Molecular systems, such as the nanoporous graphene gas separation model discussed in Chapter 3, consist of a vast number of interacting molecules. Due to the complexity associated with such systems, analytical descriptions are not possible except for the simplest (equilibrium) problems. Molecular Dynamics provides a means for *simulating* the physical motion of these molecules by treating them or their constituents as computational particles. The interactions between the particles are governed by one or more potential functions, which specify the force on each particle as a function of their position. Particle trajectories are calculated by numerically integrating the classical Newton's equations of motion for the system of interest.

MD has been extensively employed to analyze membrane gas separation applications [47, 48] and gas transport through nanoporous materials [49, 50, 51, 52], and has more recently emerged as one of the techniques of choice in modeling graphene [53]. Simulations of water and ion transport through graphene nanopores have already been achieved using MD [27, 28, 54], establishing it as the simulation technique of choice for studying the flow of gases through nanoporous graphene sheets.

This chapter describes the MD implementation in detail. The MD integration algorithm, in which molecular trajectories are calculated by numerically integrating the classical Newton's equations of motion, is then discussed. Finally, the chapter concludes with a discussion of the molecular mechanics force fields (or interatomic potentials) employed in the H_2/CH_4 and He/SF_6 simulations, and presents the relevant

potential parameters.

2.1 Sampling a Molecular System

The thermodynamic properties of interest in MD simulations, such as pressure and energy, are calculated by employing some form of averaging, introduced in statistical mechanics via the concept of ensemble average. The ensemble average of an arbitrary property A is defined as

$$\langle A \rangle_{\text{Ensemble}} = \int_{\text{p}} \int_{\text{r}} A\left(\text{p}, \text{r}\right) \rho\left(\text{p}, \text{r}\right) \text{dpdr} \tag{2.1}$$

with $\mathbf{p_i} = m_i \mathbf{v_i}$ as the linear momentum of particle i, and $\text{p} = \{\mathbf{p_i}\}$ being the set of all linear momenta in the system, for $i = 1 \ldots N$. Similarly, $\text{r} = \{\mathbf{r_i}\}$ represents the position vector of all particles. The system state is uniquely defined by the combination (p, r) since the Hamiltonian $H = H\left(\text{r}, \text{p}\right)$.

In equilibrium, the probability density function $\rho\left(\text{p}, \text{r}\right)$ is known and is given by

$$\rho\left(\text{p}, \text{r}\right) = \frac{1}{Q} \exp\left(-\frac{H\left(\text{r}, \text{p}\right)}{k_B T}\right) \tag{2.2}$$

with

$$Q = \int_{\text{p}} \int_{\text{r}} \exp\left(-\frac{H\left(\text{r}, \text{p}\right)}{k_B T}\right) \text{dpdr}. \tag{2.3}$$

In non-equilibrium situations, such as the case of gas flow through a membrane, the distribution function ρ is in general not known. Molecular Dynamics provides a resolution of this limitation, by providing a method which produces samples of this distribution making evaluation of thermodynamic, but also non-equilibrium properties a process of averaging appropriate molecular properties, namely

$$\langle A \rangle = \frac{1}{M} \sum_{i=1}^{M} A\left(\text{p}, \text{r}\right) \tag{2.4}$$

where M is the number of samples. The samples are in theory (statistical mechanics)

collected by interrogating M independent ensembles at the same instant in time. However, by using the Ergodic hypothesis

$$\langle A \rangle_{\text{Ensemble}} = \langle A \rangle_{\text{Time}}, \tag{2.5}$$

one can substitute ensemble averaging with averaging samples from a single system at different times. This process is of course only meaningful in steady processes in which $\langle A \rangle \neq \langle A \rangle(t)$. As discussed in Section 3.4, the process simulated here is time dependent (the driving force and thus the gas flux diminishes with time). As a result, samples taken at different times tend to average or "smear" the transient nature of the event. In other words, particular care needs to be taken when employing the ergodic hypothesis in transient problems, because it will only be an acceptable approximation if the sampling window is short compared to the characteristic time of variation of physical quantities. Our approach and correction for these effects are further discussed in Section 3.4.

2.2 Integration Algorithm

2.2.1 Velocity Verlet Algorithm

In molecular simulation, the goal is to predict the motion of each particle (atom or molecule), characterized by the positions $\mathbf{r}_i(t)$, velocities $\mathbf{v}_i(t)$, and accelerations $\mathbf{a}_i(t)$. Molecular dynamics generates the dynamical trajectories of a system of interacting particles by integrating Newton's equations of motion, with suitable initial and boundary conditions, and proper interatomic potentials, while satisfying macroscopic thermodynamical constraints [55]. This provides the positions $\mathbf{r}_i(t)$, velocities $\mathbf{v}_i(t)$, and accelerations $\mathbf{a}_i(t)$, all as a function of time, for all particles.

Each particle in the system, with mass m_i, must satisfy Newton's Law, $\mathbf{F}_i = m_i \mathbf{a}_i$, restated as

$$m_i \frac{d^2 \mathbf{r}_i}{dt^2} = -\frac{dU(r)}{d\mathbf{r}_i}. \tag{2.6}$$

The right hand side is the negative gradient of the potential energy, which equals to the force. The force on a particle depends on the positions of all particles. Equation (2.6) represents a system of coupled second-order nonlinear partial differential equations, corresponding to a coupled N-body problem for which no exact solution exists when $N > 2$. It is thus necessary to solve the equations by discretizing the equations in time.

The MD Simulation software, LAMMPS [56], uses the standard Velocity Verlet algorithm to calculate new positions and velocities from old positions and velocities for every particle. In the Velocity Verlet algorithm, the positions are updated after each timestep Δt using

$$\mathbf{r}_i(t + \Delta t) = \mathbf{r}_i(t) + \mathbf{v}_i(t)\,\Delta t + \frac{1}{2}\mathbf{a}_i(t)\,\Delta t^2 \tag{2.7}$$

where

$$\mathbf{v}_i(t + \Delta t) = \mathbf{v}_i(t) + \frac{1}{2}(\mathbf{a}_i(t) + \mathbf{a}_i(t + \Delta t))\,\Delta t. \tag{2.8}$$

The accelerations at time t can be obtained from the forces by considering Newton's law,

$$\mathbf{a}_i(t) = \frac{\mathbf{F}_i[\mathbf{r}_i(t)]}{m}. \tag{2.9}$$

The Velocity Verlet algorithm explicitly calculates the velocities, facilitating the application of a thermostat after Equation (2.8) to steer the system temperature towards a desired value.

2.2.2 Numerical Implementation

The Velocity Verlet algorithm forms the core of the MD simulation approach, which is presented in Figure 2-1.

The basic steps of the MD simulation algorithm can be summarized as follows:

1. Initialize the system by assigning particle positions and velocities. The initial positions of the atoms in the nanoporous graphene sheet are generated using the Carbon Nanostructure Builder plugin in the molecular visualization program

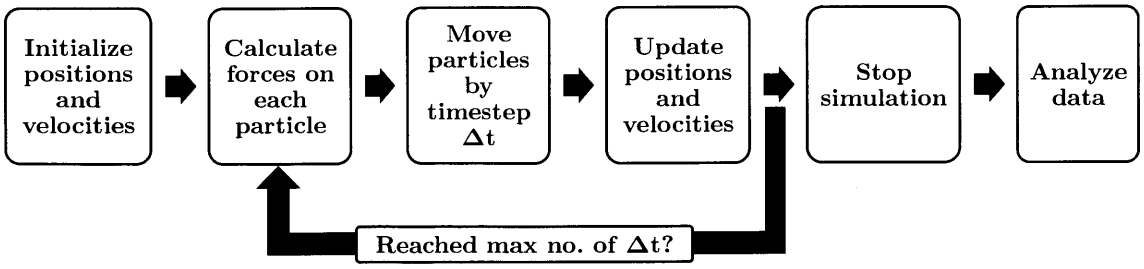

Figure 2-1: Schematic of the Molecular Dynamics numerical implementation approach.

VMD [57], as discussed in Section 3.1. Gas molecules are assigned random initial positions above the graphene. The initial velocities of the particles are drawn from a Maxwell-Boltzmann distribution by specifying a random velocity seed value.

2. Choose an interaction potential for forces, by defining an approximation of the potential energy landscape $U(r)$ that accurately describes the physics of the process being studied. The choice of potential is subsequently discussed in Section 2.3. The potential energy landscape $U(r)$ depends on the positions of all the particles in the simulation. Determine the forces on each particle, based on the calculated potential energy landscape.

3. Advance the simulation by one timestep, Δt. An appropriate timestep must be chosen, as subsequently discussed in Section 4.3. Calculate $\mathbf{r}(t + \Delta t)$ using the Velocity Verlet algorithm, Equation (2.7). Calculate $\mathbf{v}(t + \Delta t)$ using Equation (2.8), and apply thermostats (the Nosé-Hoover thermostat is applied, and is discussed further in Section 4.5) to steer the system temperature towards a desired value. Save the updated positions and velocities.

4. Run simulation for a specified number of timesteps. Designate a number of initial timesteps for equilibration, and analyze the post-equilibration molecular trajectories to determine the number of crossings. Use statistical methods to obtain flux estimates across the nanoporous graphene membranes.

2.3 Force Fields

At each integration step of the MD simulation algorithm shown in Figure 2-1, forces are required to obtain accelerations. According to Equation (2.6), the force vector is given by taking partial derivatives of the potential energy surface with respect to the atomic coordinates of the atom considered,

$$\mathbf{F}_i = -\frac{dU(r)}{d\mathbf{r}_i}. \tag{2.10}$$

The energy landscape $U(r)$ depends on the positions of all atoms. In molecular dynamics, each atom is treated as a point particle with a finite mass, in place of a three-dimensional structure [55]. Despite this simplification, the effect of electrons on atomic interactions should be as accurately described as possible by the interatomic potential. The interatomic potential aims to provide numerical or analytical expressions that estimate the energy landscape of a system of interacting particles, which is one of the fundamental inputs into molecular simulations.

A wide variety of potentials with different levels of accuracy exist. Since the atomic interactions are governed by electrons, quantum mechanics-based approaches provide the highest fidelity, but are not often used due to computational expense. As a result, sophisticated potential formulations have been empirically fitted to closely reproduce the energy landscape predicted from quantum mechanics methods, while retaining computational efficiency. The choice of interatomic potential depends on both the application and the system of interest; a brief list of the main classes of potentials is presented in ascending order of fidelity:

1. Pair Potentials (LJ [58], Morse [59])

   Pair potentials are the simplest choice for describing atomic interactions. Only pairwise interactions are considered, for which the potential energy only depends on the distance between two particles. Their main advantages are the simplicity, computational efficiency and small number of parameters required. As a result, the LJ potential is still extensively used today for a wide range of applications,

such as the modeling of noble gases. However, not all phenomena and properties (such as the elastic properties of metals) can be correctly modeled by pair potentials.

2. Multibody Potentials (EAM [60], CHARMM [61])
   In multibody potentials, the bond energy depends not only on the distance between atoms, but also on the positions of neighboring atoms within the local environment. The EAM potential is widely used to describe the elastic properties of metals. The CHARMM potential sums up both internal (covalent) and external, long-range (van der Waals, ionic and hydrogen bonding) interactions to model biological materials such as proteins.

3. Bond Order and Reactive Potentials (Tersoff [62], Brenner [63, 64], AIREBO [2], ReaxFF [65])
   Bond order potentials describe the bond strength between two atoms based on the local environment, but also include specific terms to specify the directional dependence of the bonding. They are particularly suitable for describing the forces in covalently-bonded materials, where the bonds have a strong directional dependence. Hence, bond order potentials are very useful in describing carbon-based materials [55] such as carbon nanotubes and graphene. Reactive potentials such as AIREBO and ReaxFF are highly sophisticated potentials that are derived by fitting against quantum mechanical data from DFT simulations. Hence, they are able to describe bond formation and rupture, in addition to nonbonded interactions. Due to the complexities of the force field expressions, reactive force fields are between 50 to 100 times more expensive than nonreactive force fields, but are several orders of magnitude faster than DFT calculations that would be able to describe bond formation and rupture.

In this thesis, the AIREBO potential is chosen to describe the intermolecular interactions in the H_2/CH_4/graphene system. A hybrid potential consisting of the AIREBO (for graphene) and Lennard-Jones (LJ) potentials (for the gas species) is chosen to describe the intermolecular interactions in the He/SF_6/graphene system.

2.3.1 AIREBO Potential for H_2/CH_4 Simulations

The Adaptive Intermolecular Reactive Empirical Bond Order (AIREBO) potential is widely used to describe hydrocarbon systems [66] containing carbon nanostructures such as graphene and carbon nanotubes [67, 68]. It is well suited for describing the intermolecular interactions in the H_2/CH_4/graphene system for a number of reasons.

Firstly, the reactivity of the AIREBO potential allows for the formation and dissociation of covalent bonds throughout the simulation. The local coordination environment of each atom is used to modify the strength of conventional pairwise terms. Thus, individual atoms are not constrained to remain attached to specific neighbors, or maintain a particular hybridization state or coordination number [2]. Hence, the AIREBO potential can provide a realistic description of the covalent bonding in the graphene sheet (both in the vicinity of the nanopore and away from it) and the gas species. Hence, the dynamics of the graphene sheet can be studied throughout the simulation, and any transport of gas molecules through the nanopores would take into account the dynamical effects of graphene.

Secondly, the adaptive nature of the AIREBO potential allows it to accurately describe and distinguish between nonbonded intermolecular interactions and reactive, covalent bonding interactions [2]. The AIREBO potential is able to capture the long-ranged intermolecular interactions between the gas species and the graphene, providing a physically accurate model for the gas separation process. In this respect, the AIREBO potential is more useful than the REBO potential developed by Brenner [63], which is exclusively short-ranged - two atoms interact directly only if they are separated by a distance less than a covalent bonding cutoff (e.g., 2.0 Å for C-C bonds).

Furthermore, the AIREBO potential is completely parameterized for systems containing C and H atoms, such as the H_2/CH_4/graphene system of interest. The AIREBO potential parameters are fully specified in a LAMMPS source file, and are thus easily implemented in a simulation.

A description of the key equations and parameters follows. The equations and parameters have been copied directly from Stuart et al. [2], and are reproduced in this

thesis to develop an appreciation for the advantages and limitations of the potential, and also guide future work.

The AIREBO potential can be represented by a sum over pairwise interactions, including covalent bonding interactions (REBO terms that correspond to [63]), LJ terms, and torsion interactions:

$$E = \frac{1}{2}\sum_{i}\sum_{j\neq 1}\left[E_{ij}^{\mathrm{REBO}} + E_{ij}^{\mathrm{LJ}} + \sum_{k\neq i,j}\sum_{l\neq i,j,k} E_{kijl}^{\mathrm{tors}}\right]. \tag{2.11}$$

Each pair of covalently-bonded atoms interacts via the REBO term for covalent bonding,

$$E_{ij}^{\mathrm{REBO}} = V_{ij}^{\mathrm{R}} + b_{ij}V_{ij}^{\mathrm{A}}, \tag{2.12}$$

where V_{ij}^{R} and V_{ij}^{A} are the repulsive and attractive pairwise potentials determined by the type of atom (carbon or hydrogen) i or j, and the distance r_{ij} between the two atoms. The value of the E_{ij}^{REBO} term depends on the position and chemical identity of atoms close to the i-j bond through the bond order term, b_{ij}.

The repulsive REBO term in Equation (2.12) is:

$$V_{ij}^{\mathrm{R}} = w_{ij}(r_{ij})\left[1 + \frac{Q_{ij}}{r_{ij}}\right]A_{ij}e^{-\alpha_{ij}r_{ij}}, \tag{2.13}$$

where the parameters Q_{ij}, A_{ij}, and α_{ij} depend on the atom types i and j. Values for these and all other potential parameters are given in Table 2.1. The w_{ij} term switches off REBO interactions when atom pairs exceed typical bonding distances, as the REBO term is short-ranged.

The attractive REBO term in Equation (2.12) is:

$$V_{ij}^{\mathrm{A}} = -w_{ij}(r_{ij})\sum_{n=1}^{3} B_{ij}^{(n)}e^{-\beta_{ij}^{(n)}r_{ij}}, \tag{2.14}$$

where the parameters $B_{ij}^{(n)}$ and $\beta_{ij}^{(n)}$ are given in Table 2.1. Once again, the w_{ij} term switches off REBO interactions when atom pairs exceed typical bonding distances.

The b_{ij} term specifies the "bond order" for the interaction between atoms i and

j, and is a means of modifying the strength of a bond due to changes in the local environment. The formulation of the b_{ij} term imposes an energy penalty on bonds that are too close to one another, rotation around multiple bonds, and takes into account radical and conjugation effects.

The LJ contribution to the i-j pair energy (i.e. the LJ term) in Equation (2.11) is:

$$E_{ij}^{\mathrm{LJ}} = S(t_r(r_{ij}))\, S\big(t_b\big(b_{ij}^*\big)\big)\, C_{ij} V_{ij}^{\mathrm{LJ}}(r_{ij}) + [1 - S(t_r(r_{ij}))]\, C_{ij} V_{ij}^{\mathrm{LJ}}(r_{ij})\,, \tag{2.15}$$

which includes the traditional LJ term

$$V_{ij}^{\mathrm{LJ}}(r_{ij}) = 4\epsilon_{ij}\left[\left(\frac{\sigma_{ij}}{r_{ij}}\right)^{12} - \left(\frac{\sigma_{ij}}{r_{ij}}\right)^{6}\right], \tag{2.16}$$

modified by several sets of switching functions $S(t)$. The switching functions can be used to switch off the LJ interaction according to three criteria. The decision is made adaptively, depending on: (i) the distance separating the pair of atoms in question, (ii) the strength of any bonding interaction between them, and (iii) the network of bonds connecting them. The distance between a pair of atoms affects the strength of their LJ interaction through the $S(t_r(r_{ij}))$ term in Equation (2.15). The strength of any bonding interaction between a pair of atoms affects the strength of their LJ interaction through the $S\big(t_b\big(b_{ij}^*\big)\big)$ term in Equation (2.15). $t_r(r_{ij})$ and $t_b\big(b_{ij}^*\big)$ are scaling functions, while the b_{ij}^* term is a bond order term for the nonbonded portions of the AIREBO potential that is analogous to the b_{ij} term in the REBO term. The parameters σ_{ij} and ϵ_{ij} are given in Table 2.1.

The contribution of dihedral angles (i.e. the torsional energy term) to the total energy in Equation (2.11) is:

$$E_{kijl}^{\mathrm{tors}} = w_{ki}(r_{ki})\, w_{ij}(r_{ij})\, w_{jl}(r_{jl})\, V^{tors}(\omega_{kijl})\,, \tag{2.17}$$

where

$$V^{tors}(\omega_{kijl}) = \frac{256}{405}\,\epsilon_{kijl}\cos^{10}(\omega_{kijl}/2) - \frac{1}{10}\,\epsilon_{kijl}. \tag{2.18}$$

The parameter ϵ_{kijl} is given in Table 2.1. Also, the use of bond weights such as $w_{ij}(r_{ij})$ ensures that the torsional energy associated with a given dihedral angle will be removed smoothly as any of the constituent bonds are broken.

Table 2.1: Parameters for the AIREBO potential, obtained from Stuart et al. [2]. "..." indicates that the parameter is not specified. The ρ_{ij} parameter is not discussed in the thesis but is provided for completeness. (Refer to Equation A14 of Stuart et al.)

	Value			
Parameter	CC	CH	HH	Eqn. No.
Q_{ij} (Å)	0.313460	0.340776	0.370471	(2.13)
α_{ij} (Å^{-1})	4.7465391	4.1025498	3.5362986	(2.13)
A_{ij} (eV)	10953.544	149.94099	32.817356	(2.13)
$B_{ij}^{(1)}$ (eV)	12388.792	32.355187	29.632593	(2.14)
$B_{ij}^{(2)}$ (eV)	17.567065	...	...	(2.14)
$B_{ij}^{(3)}$ (eV)	30.714932	...	...	(2.14)
$\beta_{ij}^{(1)}$ (Å^{-1})	4.7204523	1.4344581	1.7158922	(2.14)
$\beta_{ij}^{(2)}$ (Å^{-1})	1.4332132	...	...	(2.14)
$\beta_{ij}^{(3)}$ (Å^{-1})	1.3826913	...	...	(2.14)
ρ_{ij} (Å)	...	1.09	0.7415887	-
ϵ_{ij} (eV)	0.00284	$\sqrt{\epsilon_{\mathrm{CC}}\epsilon_{\mathrm{HH}}}$	0.00150	(2.16)
σ_{ij} (Å)	3.40	$\frac{1}{2}(\sigma_{\mathrm{CC}} + \sigma_{\mathrm{HH}})$	2.65	(2.16)
$\epsilon_{i\mathrm{CC}j}$ (eV)	0.3079	0.1787	0.1250	(2.18)

2.3.2 Hybrid Potential for He/SF_6 Simulations

While the interaction potential in the graphene sheet can be specified by the AIREBO potential, interactions concerning He and SF_6 molecules need to be modeled. Hence, a hybrid potential needs to be specified for the He/SF_6/graphene system, with the AIREBO potential describing interactions in graphene, and the 'site-site' Lennard-Jones potential describing interactions for He and SF_6.

The interaction between the nuclei and electronic charge clouds of a pair of molecules i and j is a complicated function of relative positions $\mathbf{r}_i$, $\mathbf{r}_j$ and orientations $\mathbf{\Omega}_i$, $\mathbf{\Omega}_j$. In the 'site-site' model, each molecule is modeled based on the positions and sizes of the constituent atoms, and the total interaction $V(\mathbf{r}_{ij}, \mathbf{\Omega}_i, \mathbf{\Omega}_j)$ is a sum of pairwise contributions from distinct sites a in molecule i, at position $\mathbf{r}_{ia}$, and b in molecule j, at position $\mathbf{r}_{jb}$ [69],

$$V(\mathbf{r}_{ij}, \mathbf{\Omega}_i, \mathbf{\Omega}_j) = \sum_a \sum_b V_{ab}(r_{ab}) \tag{2.19}$$

where a and b can either take the values of 1 (He) or 1 through 7 (SF_6), V_{ab} is the pair potential acting between sites a and b, and $r_{ab} = |\mathbf{r}_{ia}\text{- }\mathbf{r}_{jb}|$, the inter-site separation.

Each short-range site-site interaction can be modeled using a Lennard-Jones potential [69]. Interactions between pairs of identical atoms in different molecules have been characterized, and the LJ energy (ϵ) and length (σ) parameters have been tabulated for a large number of elements. Interactions between unlike atoms in different molecules are usually approximated using the Lorentz-Berthelot mixing rules if specific data is not found in the literature. For example, the LJ energy and length parameters for S-F interactions in SF_6 can be calculated from the energy and length parameters for the S-S and F-F interactions using

$$\sigma_{\mathrm{SF}} = \frac{1}{2}\left[\sigma_{\mathrm{SS}} + \sigma_{\mathrm{FF}}\right] \tag{2.20}$$

and

$$\epsilon_{\mathrm{SF}} = \left[\epsilon_{\mathrm{SS}}\epsilon_{\mathrm{FF}}\right]^{1/2}. \tag{2.21}$$

LJ energy (ϵ) and length (σ) parameters for pairs of identical atoms are obtained from literature. The LJ parameters for C-S and C-F interactions are obtained from the C-C LJ parameters of $\epsilon = 2.413 \times 10^3$ eV and $\sigma = 3.40$ Å respectively. The LJ parameters for SF_6 are obtained from a "seven-sites without charges" potential model [70] that accurately predicts the physical properties of SF_6. LJ parameters for all pairwise interactions present in the He/SF_6/graphene system are presented in

Table 2.2.

Table 2.2: LJ interaction parameters for the hybrid potential. LJ parameters are not listed for the C-C bond because the AIREBO formulation is used to describe graphene.

	Value		
Parameter	$\epsilon\,(\times 10^{-3}\,\text{eV})$	$\sigma\,(\text{Å})$	Source
C-C	-	-	[2]
He-He	0.8801	2.56	[71]
S-S	14.123	3.246	[70]
F-F	2.347	2.954	[70]
C-He	1.611	2.971	L-B
C-S	5.838	3.323	L-B
C-F	2.380	3.177	L-B
He-S	3.526	2.903	L-B
He-F	1.437	2.757	L-B
S-F	5.758	3.100	L-B

In addition, bond and angle vibrations within the SF_6 molecule are modeled using a harmonic type potential [70],

$$U_{intra} = \sum_{bonds} K_r \left(r - r_0\right)^2 + \sum_{angles} K_\theta \left(\theta - \theta_0\right)^2, \tag{2.22}$$

where r_0 and θ_0 are the S-F bond and F-S-F angle equilibrium averages respectively. The parameter values are: $K_r = 7.1874$ eV/Å^2, $r_0 = 1.565$ Å; $K_\theta = 3.1856$ eV/rad^2, $\theta_0 = 90°$. It is noteworthy that angles are specified in radians for K_θ and degrees for θ_0.

Chapter 3

Nanoporous Graphene Gas Separation Model

This chapter describes the modeling aspects of the setup used to simulate gas transport through nanoporous graphene membranes. It is complemented by Chapter 4, which discusses the MD simulation parameters in the context of numerical implementation in LAMMPS. The computational modeling of nanoporous graphene and the gas species is first described. Next, the physical setup and key features of the simulation box are explained. Finally, a method for obtaining meaningful, accurate data on gas flow rates is discussed.

3.1 Modeling of Nanoporous Graphene

Visual Molecular Dynamics (VMD) [57], an open-source molecular visualization program, is employed to model a nanoporous graphene sheet. A single layer graphene sheet comprising 416 carbon atoms is generated using the Carbon Nanostructure Builder plugin, by specifying an edge length of 3 nm along both the x and y-directions, and an 'armchair' edge configuration. The atomic coordinates are saved in a .pdb file, which is compatible with most major molecular visualization software. Alternatively, the atomic coordinates of graphene can be generated using a MATLAB code created for this purpose.

Nanoporous graphene is modeled by selectively removing atoms to create pores in VMD's Tk Console. The resulting .pdb file is subsequently converted by VMD into a format that is compatible with the MD simulation software, LAMMPS. For H_2/CH_4 simulations, only the atomic coordinates are written to the LAMMPS input data file, as the potential description does not require treatment of bonds and angles, and the *atomic* input style would suffice. On the other hand, the potential description in He/SF_6 simulations includes bonds and angles. Hence, information about bonds and angles are written to the LAMMPS input data file in addition to atomic coordinates, and the *angle* input style is necessary.

The pore size required to separate a mixture of gases into its constituent species depends on the kinetic diameters of the constituent species. The kinetic diameter is the smallest effective dimension of a given molecule, and is the characteristic length for determining the permeability of a molecule through nanopores. Table 3.1, with data adapted from literature [72], presents the kinetic diameters and molecular weights of gas molecules of interest.

Table 3.1: Kinetic diameter and molecular weight of selected gas molecules

Permeating Gas	He	H_2	CH_4	SF_6
Kinetic Diameter (Å)	2.6	2.89	3.8	5.5
Molecular Weight	4	2	16	146

Simulations are performed on a range of pore sizes to elucidate the effect of pore size on gas transport. In this thesis, pore sizes are denominated by lattice units (of area), where 1 lattice unit refers to the hexagonal "ring" formed by 6 carbon atoms. Although the pore size could be quantified using the number of carbon atoms removed, here we use the pore area because it more directly relates to the area through which gas molecules can pass. In addition, atoms are discretely removed from the graphene lattice to create regularly-shaped circular or elliptical pores. This attempt to control for pore geometry allows the effect of pore size on gas transport to be more clearly elucidated.

Since SF_6 has a larger kinetic diameter than CH_4, the expected maximum pore size that effectively blocks out the larger species is larger for He/SF_6 separation than for H_2/CH_4 separation. Hence, larger pore sizes are investigated for He/SF_6 separation. Four different pore sizes, ranging from 6 to 14 lattice units, are investigated for H_2/CH_4 separation, as presented in Figure 3-1. For He/SF_6 separation, five different pore sizes, ranging from 7 to 16 lattice units, are investigated (see Figure 3-2).

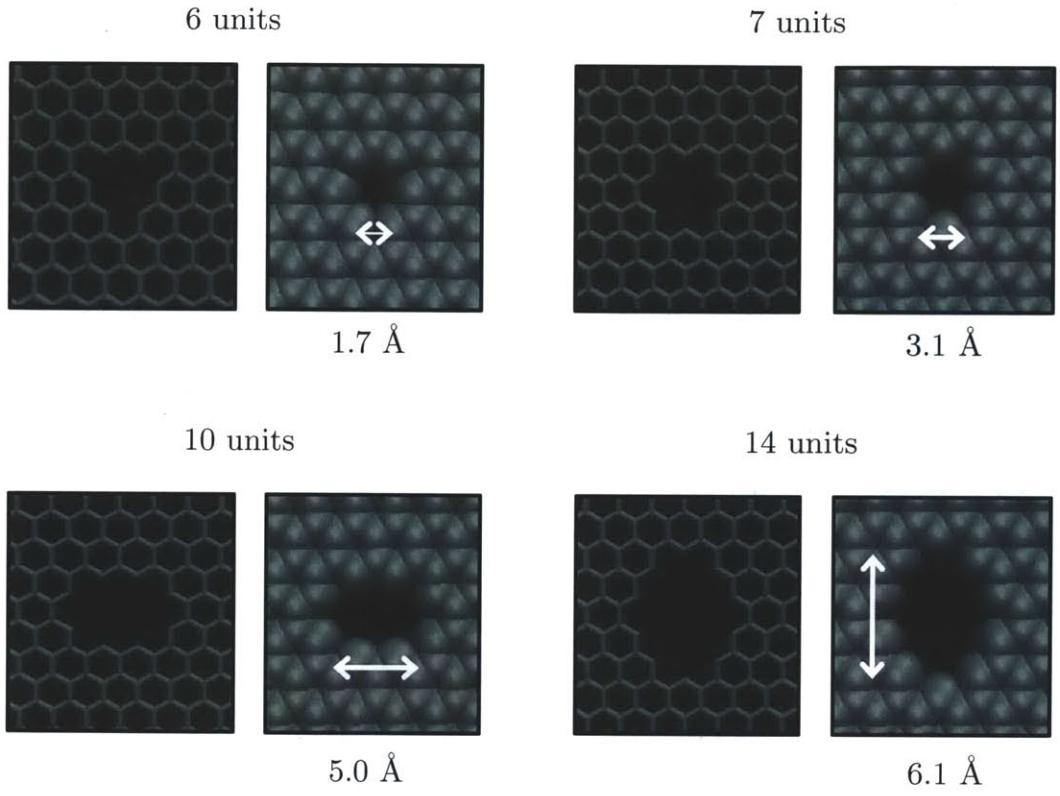

Figure 3-1: Four different pore sizes, ranging from 6 to 14 lattice units, are investigated for H_2/CH_4 separation. Each nanopore is visualized in two ways: the image on the left shows the bonds in graphene, and the image on the right shows the VDW radii of the atoms comprising the pore. The larger dimension of each pore is labeled.

3.2 Modeling of Gas Species

The LAMMPS input data file contains information about the initial coordinates of every atom in the simulation. A list of initial atomic coordinates is generated by

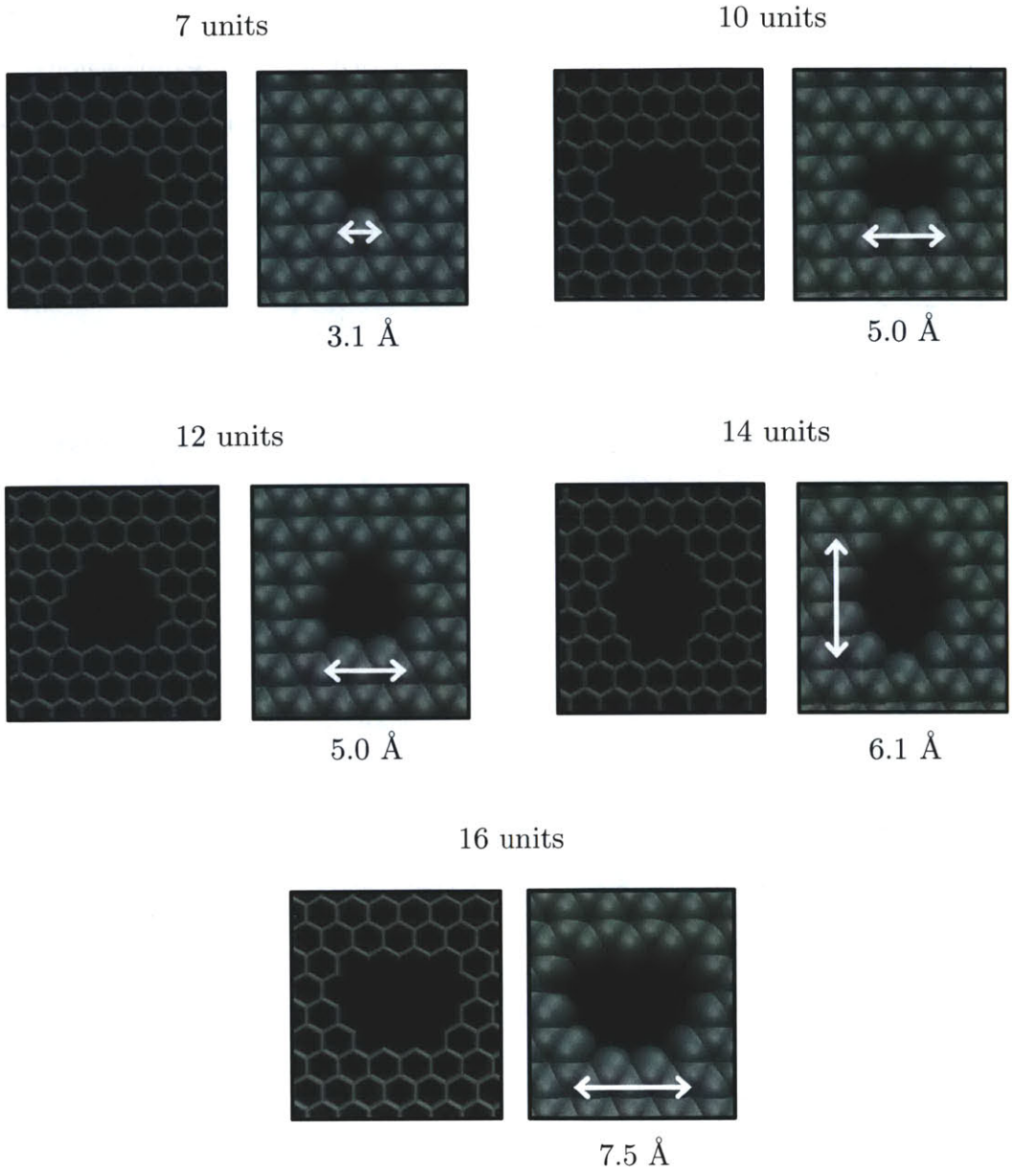

Figure 3-2: Five different pore sizes, ranging from 7 to 16 lattice units, are investigated for He/SF_6 separation. Each nanopore is visualized in two ways: the image on the left shows the bonds in graphene, and the image on the right shows the VDW radii of the atoms comprising the pore. The larger dimension of each pore is labeled.

considering the molecular structure of the respective species. The initial coordinates reflect equilibrium bond lengths and angles; additionally, LAMMPS employs energy minimization algorithms listed in Section 4.3 to adjust the atomic coordinates before the simulation is run.

Table 3.2 presents the molecular geometry of gas molecules that are of interest.

Table 3.2: Molecular geometry of selected gas molecules

Molecule	Geometry	Bond Length (Å)	Bond Angle	Source
He	Monatomic	-	-	NIST
H_2	Linear	0.741	180°	NIST
CH_4	Tetrahedral	1.087	109.47°	NIST
SF_6	Octahedral	1.565	90°	[70]

No additional information about the bonds in H_2 and CH_4 need to be specified as an input to LAMMPS, as the latter contains default AIREBO potential interaction parameters, which are used for the H_2/CH_4 simulations. On the other hand, the potential formulation for the He/SF_6 simulations is more complicated; as a result, default parameter values are not included in LAMMPS and must be specified. As discussed in Section 2.3.2, bond and angle vibrations within the SF_6 are modeled as harmonic bonds, which are springs with associated stretching and bending stiffnesses. The bond stiffness parameters are provided in Section 2.3.2.

3.3 Simulation Box Setup

The graphene sheet with the relevant nanopore size, as modeled in Section 3.1, is then placed horizontally (i.e. in the x-y plane) in the middle of the simulation box. One hundred molecules of each gas species that comprise the gas mixture are randomly positioned above the nanoporous graphene sheet. The size of the simulation box is

calculated using the ideal gas equation

$$pV = Nk_BT, \tag{3.1}$$

where p is the partial pressure of each gas species (1 atm), V is the simulation box volume, N is the number of particles, k_B is the Boltzmann constant, and T is the temperature. Since the length and width of the simulation box correspond to the length of each side of the nanoporous graphene sheet (3 nm), the simulation box extends 450 nm both above and below the graphene sheet to obtain the desired volume and gas partial pressures.

Periodic boundary conditions are applied in the plane of the graphene sheet. This allows the graphene sheet unit cell, a 3 nm $\times$ 3 nm graphene sheet with the desired subnanometer pore size, to be replicated infinitely as a nanoporous graphene sheet while neglecting edge dynamics [73]. Since one pore is present for each 9 nm^2 of graphene, the pore coverage is proportional to pore size. The pore coverage corresponding to the modeled nanoporous graphene sheets ranges between 1 % to 4.5 %. To avoid vertical displacement of the entire graphene sheet due to collisions with the gas molecules, the position of one atom in the sheet is fixed. This atom is situated as far away as possible from each nanopore to avoid interfering with the dynamics of the atoms in the vicinity of the nanopore.

Figure 3-3 illustrates a simulation box for H_2/CH_4 separation, as rendered in VMD using Tachyon Ray Tracing [74]. It should be noted that Figure 3-3 depicts gas partial pressures that are much higher than 1 atm for illustrative purposes.

3.4 Gas Flux Measurement

The simulations were run in LAMMPS for a duration of between 20 ns to 40 ns, including a 6 ns equilibration period of 30 $\times$ 10^6 timesteps. The total simulation length is 3 orders of magnitude longer than the simulations performed by Jiang et al. [24]. MD simulations of each pore size are performed with 16 replicates that

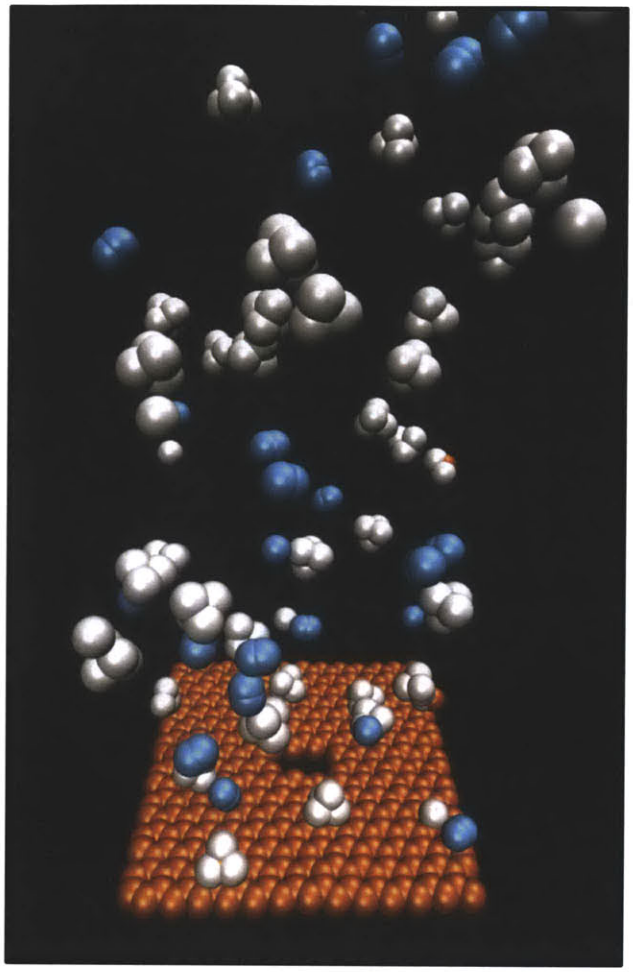

Figure 3-3: Illustration of simulation box for the separation of H_2 (in blue) from CH_4 (in white) using a nanoporous graphene membrane (in orange). The pictured pore has a size of 10 lattice units, which corresponds to a porosity of 2.4%.

are initialized with different and random velocities. This allows a large number of molecular trajectories to be sampled, in order to predict gas transport rates with low uncertainty, as the associated uncertainty varies with the inverse root of the number of independent samples. The simulation temperature is held constant at 300 K using a Nosé-Hoover thermostat [75, 76], which is described more extensively in Section 4.5.

Throughout the course of the simulation, LAMMPS prints out the coordinates of each atom at specifiable time intervals. Molecular crossings can be identified either by visualizing the output in VMD, or by analysis of the output coordinate file to

identify molecules with a negative z-coordinate. The number of post-equilibration-phase crossings is counted, then normalized by the size of the graphene sheet (9 nm^2) and simulation duration to obtain the flux, with units of [$mol/m^2\,s$]. The flux is further normalized by the driving pressure difference to yield the permeability, with units of [$mol/m^2\,s\,Pa$].

An initial pressure difference of 1 atm (a partial pressure of 1 atm above the graphene and 0 atm below the graphene) drives the flow of the individual gas species. However, the partial pressure of the permeating species in the upper chamber drops while that in the lower chamber rises, as molecules permeate the graphene sheet when the simulation progresses. To limit the effect of this pressure drop as much as possible, we measure the gas flux at early times (following an appropriate equilibration period); at the same time we allow for a sufficient number of molecular crossings for a statistically significant sample. The flux is estimated by measuring the time required for the first 20 net crossings to occur, or if the total simulation time is exceeded before this number of crossings occurs, the net number of crossings occurring in this time. However, because 20 molecular crossings correspond to 20% of the total number of molecules of each species, we also apply a correction that takes into account the fact that the average pressure difference during the course of the simulation is lower than the initial driving force of 1 atm. For any gas species A, we use the estimate

$$\text{Molar Flux of A at 1 atm} = \text{Calculated Molar Flux of A} \times \frac{100}{100 - (n_i + n_f)} \quad (3.2)$$

where n_i and n_f are the net number of molecules of A that have crossed the graphene sheet at the end of the equilibration phase and analysis period, respectively. We note that the net flux is calculated based on the *net* number of molecules crossing the membrane - if 10 molecules of A pass from the upper chamber to the lower chamber, with a back flow of 2 molecules into the upper chamber, the net number of molecules of A that have crossed the graphene sheet is 8.

Chapter 4

LAMMPS Molecular Dynamics Simulation Details

In this thesis, simulations were performed using the November 9, 2011 release of LAMMPS "Large-scale Atomic/Molecular Massively Parallel Simulator" - a classical MD program from Sandia National Laboratories. It implements the MD simulation algorithm shown in Figure 2-1, and is capable of running on single processors or in parallel.

Two main inputs are required in LAMMPS: (1) An input data file containing information about atom types, initial coordinates, bonds, angles, dihedral and improper quadruplets (the last four items are only required in certain types of simulations), and (2) an input script. A LAMMPS input script is typically sub-divided into 4 parts:

1. Initialization

   Set parameters that need to be defined before atoms can be read from the input data file.

2. Atom Definition

   Atom types, initial coordinates and molecular topology information such as bonds, angles, dihedral and improper quadruplets are read from an input file. Alternatively, atoms can be directly created on a lattice by specifying relevant rules, but this is not performed in this thesis.

3. Settings

   Once the atoms and molecular topology are defined, many types of settings can be specified. They include force field coefficients, simulation parameters, fixes (boundary conditions and integration methods), peripheral computations and output options.

4. Run Simulation

   Perform energy minimization, and run the simulation.

This chapter describes the LAMMPS MD simulation parameters with an intent to guide future work in this field. The following sections discuss the commands (in bold, small letters at the top of each section and in quotation marks in the text) and associated arguments (in quotation marks) that are specified in each part of the LAMMPS input script, in the context of the H_2/CH_4 and He/SF_6 simulations. Much of the description has been adapted from the LAMMPS Manual, and is presented in this thesis as a guide to building a functional LAMMPS input script. In general, both simulations are very similar, and the parameters for both simulations are the same unless explicitly discussed. However, a key difference is that the hybrid potential specification in the He/SF_6 simulations requires more information to be provided about the initial molecular topology, and interaction parameters must be provided in the input script.

4.1 Initialization

units

This command sets the style of units for the simulation. It determines the units of all the quantities specified in the input script and data file, as well as quantities output to the screen, log file, and dump file. The "units" style chosen is "metal", as the parameters for the AIREBO potential file provided with LAMMPS are parameterized with "metal" units. The "metal" style uses conventional MD units:

- mass = g/mole

- distance = Å
- time = ps
- energy = eV
- temperature = K

atom_style

This command defines the style of atoms to use in a simulation, which affects what parameters are stored by each atom, and what parameters are read from the input data file. The "atom_style" chosen for the H_2/CH_4 simulations is "atomic", which does not read information about bonds and angles from the input data file. It is chosen as the AIREBO potential can determine bonds and angles by itself. The "atom_style" chosen for the He/SF_6 simulations is "angle", which reads information about bonds and angles from the input data file. This is necessary for specifying the geometry of the SF_6 molecule, which is not described by the AIREBO potential.

dimension

This command sets the dimensionality of the simulation, which is "3".

boundary

This command specifies the boundary conditions for the global simulation box in each dimension. The "p p f" style is chosen, indicating that the box is periodic in the x and y dimensions, but not in the z dimension. Periodic boundary conditions mean that particles can exit one end of the box and re-enter from the other end when they interact across the boundary, as the simulation box is replicated infinitely in the plane of the graphene sheet. This is necessary for the simulation of a nanoporous graphene sheet from a 3nm $\times$ 3nm sheet with a single pore, as noted in Section 3.3.

4.2 Atom Definition

read_data

This command reads the information LAMMPS needs to run a simulation from the data file. The data file for the H_2/CH_4 simulations contains atomic masses and initial coordinates, while the data file for the He/SF_6 simulations contains atomic masses, initial coordinates and molecular topologies including bond and angle information. The data file name is provided as an argument to the "read_data" command.

group

This command identifies a collection of atoms as belonging to a group, to which an ID is assigned. The group ID can then be used in commands such as "fix", "compute" and "velocity" to act on those atoms together. In general, atoms of the same type that belong to the same type of molecule are grouped together. However, an additional group "nail" is defined, which contains one atom within the graphene sheet that is frozen to avoid vertical displacement of the entire sheet, as discussed in Section 3.3.

4.3 Settings: Simulation Parameters

neighbor; neigh_modify

These commands set parameters that affect the building and use of pairwise neighbor lists, which LAMMPS employs to keep track of nearby particles for computational efficiency. All atom pairs within a neighbor cutoff distance equal to their force cutoff plus the skin distance are stored in the neighbor list. The "nsq" style is chosen under "neighbor", which scales as $(N/P)^2$, where N = total number of atoms and P = number of processors. However, an alternative style "bin" that creates the neighbor list by binning is recommended, as it scales as N/P and runs about 14% faster than the "nsq" style. The skin distance is set as "5.0"(Å), which is sufficiently large to avoid dangerous builds that may indicate problems with neighbor list setup. The arguments for "neigh_modify" are "delay 0 every 1 check yes", which instructs

LAMMPS to build the neighbor list on every step if some atom has moved more than half the skin distance since the last build. These parameters were also iteratively chosen to avoid dangerous builds from occurring.

timestep

This command sets the timestep for the MD simulation as "0.0002" (ps) or 0.2 fs. The chosen timestep must be small enough to avoid discretization errors and must hence be smaller than the inverse of the fastest vibrational frequency in the system, but also large enough for the total simulation duration to access the desired phenomena in a meaningful way. Typical timesteps in MD simulations are on the order of 1 fs, while Stuart et al. reports a timestep of 0.5 fs in the original literature on the AIREBO potential [2]. However, a smaller timestep of 0.2 fs was chosen for the simulation to remain stable, and reduce discretization errors over the lengthy duration of the simulations performed in this thesis. The timestep can be extended using algorithms such as 'SHAKE' [77], which fix the vibrations of the fastest atoms into place. However, the 'SHAKE' algorithm is not used in this thesis as the effect of atomic vibrations on transport through nanopores may not be negligible. Furthermore, the geometry of SF_6 is too complicated for the implementation of the 'SHAKE' algorithm.

min_style

This command specifies an energy minimization algorithm to use. The "sd" or steepest descent algorithm is chosen due to its robustness. At each iteration, the search direction is set to the downhill direction corresponding to the force vector.

4.4 Settings: Force Field Coefficients

In general, the force calculation step of the MD simulation algorithm shown in Figure 2-1 takes up the vast majority of the simulation time and computational resources.

pair_style; pair_coeff

This command sets the formula and coefficients that LAMMPS uses to compute pairwise interactions. In LAMMPS, pair potentials are defined between pairs of atoms that are within a cutoff distance.

The "pair_style" chosen for the H_2/CH_4 simulations is "airebo", with a cutoff scale factor of "3.0" σ for the LJ term of the AIREBO potential shown in Equation (2.11). As discussed in Section 2.3.1, the LJ term describes longer-ranged interactions, while the REBO term describes short-ranged C-C, C-H and H-H interactions. The potential formulation specifies the REBO cutoff to be 2 Å, and this parameter is listed in the default AIREBO parameter file. The location of the AIREBO parameter file is specified as an argument for the "pair_coeff" command, together with information that identifies the atom types in the LAMMPS input coordinate file.

The "pair_style" chosen for the He/SF_6 simulations is "hybrid". The AIREBO component of the hybrid potential formulation bears the same cutoff scale factor as the H_2/CH_4 simulations. However, the lack of a default parameter file for the hybrid potential means that interaction parameters for the LJ part of the potential (with a cutoff distance argument of "5" Å) must be provided as an input to LAMMPS. The interaction parameters for the bonds between any permutation of atoms in the He/SF_6/graphene system are found in Table 2.2.

bond_style; bond_coeff; angle_style; angle_coeff

These commands set the formulae and coefficients LAMMPS uses to compute bond interactions between pairs of atoms and angle interactions between triplets of atoms which remain in force for the duration of the simulation. These commands only need to be defined for the He/SF_6 simulations, as the AIREBO potential used in the H_2/CH_4 simulations can determine bonds and angles by itself.

Bond and angle vibrations within the SF_6 molecule are modeled in literature [70] using a harmonic type potential, according to Equation 2.22. Hence, the arguments for "bond_style" and "angle_style" are both "harmonic". The arguments for "bond_-

coeff" are "7.1874" (eV/Å^2) and "1.565" (Å), while the arguments for "angle_coeff" are "3.1856" (eV/rad^2) and "90" (°), based on the parameters discussed in Section 2.3.2.

4.5 Settings: Fixes

In LAMMPS, a "fix" is any operation that is applied to the system during timestepping or minimization, including integration, thermostatting, applying constraint forces to atoms and enforcing boundary conditions. Fixes are applied to groups of atoms by using the following commands:

fix nvt

This command performs time integration on the Nosé-Hoover non-Hamiltonian equations of motion, which are designed to generate positions and velocities sampled from the canonical (NVT) ensemble. Thermostatting is achieved by adding dynamic variables which are coupled to the particle velocities. By default, LAMMPS creates a chain of 3 thermostats coupled to the particle thermostat, for which the equations of motion are described in Shinoda et al [78]. The thermostat is applied to only the translational degrees of freedom by using the "temp" argument, with a desired temperature at each timestep corresponding to a ramped value during the run from T_{start} to T_{stop}, and a damping parameter T_{damp} that determines how rapidly the temperature is relaxed. Since the desired simulation temperature is constant, both T_{start} and T_{stop} are specified to be "300" (K). T_{damp} is set as "0.01" (ps) for the H_2/CH_4 simulations, and "0.02" (ps) for the He/SF_6 simulations. A recommended choice of T_{damp} is 100 timesteps, which in the case of these simulations is 0.02 ps. The slightly smaller T_{damp} parameter for the H_2/CH_4 simulations did not result in wild temperature fluctuations, and is thus acceptable.

fix setforce

This command sets each component of force on each atom in the group to a specified value, erasing all previously computed forces on the atom. It is used to freeze atoms

in the group "nail", by setting all three components of its force to a value of "0.0".

In some reported simulations [28], the carbon atoms that comprise the graphene sheet are frozen in their lattice position to prevent out-of-plane displacement, and perhaps reduce computational expense in order to achieve a longer simulation duration. However, molecular dynamics simulations are successful only when detailed atomistic models are used for both the membrane and the gas molecules, and if the thermal vibrations of the membrane are taken into consideration [14, 47]. As a result, we only froze one graphene atom, as discussed in Section 3.3.

fix wall/reflect

This command bounds the simulation box with walls which reflect particles in the specified group when they attempt to move through them. While periodic boundary conditions are applied in the directions corresponding to the plane of the graphene sheet, reflecting walls are implemented at the upper and lower bounds of the simulation box to conserve particles that attempt to leave the box. Particles that are moving to a z-coordinate (i.e. in the direction normal to the graphene sheet) that is less than the lower wall position or higher than the upper wall position are reflected back into the simulation box by specifying the "zlo EDGE zhi EDGE" arguments, where "EDGE" defines the position of the wall to be the edge of the simulation box. This boundary condition is applied to "all" atom types.

4.6 Settings: Output Options

thermo, thermo_style

The "thermo" command is used to compute and print thermodynamic information on timesteps that are a multiple of "100000" and at the beginning and end of a simulation. The "thermo_style" command is used to set the style and content for printing thermodynamic data to the log file. A "custom" format is chosen, in order for essential content to be manually specified: "step", "temp", "etotal", "pe" and "ke" print the timestep, temperature, total energy, potential energy and kinetic energy

respectively. It is important for information about the temperature and energy to be displayed, in order to gauge the effectiveness of the thermostat.

dump

This command is used to dump a snapshot of specific atom quantities to an output file every "10000000" timesteps. A "custom" format is chosen, in order for essential content to be manually specified: "id", "type", "x", "y" and "z" print the number, type and coordinates of each atom respectively to a trajectory file that can be visualized in VMD.

4.7 Running the Simulation

minimize

This command performs an energy minimization on the system by iteratively adjusting atom coordinates. Iterations are terminated when one of the stopping criteria is satisfied, or the number of iterations and force evaluations exceed a specified value. The arguments of the "minimize" command are "1.0e-12", "1.0e-12", "2000" and "2000", which refer to the stopping tolerance for energy, force, maximum number of iterations and force evaluations respectively. The first criterion is met when the energy change between successive iterations divided by the energy magnitude is less than or equal to the tolerance - one part in 10^{12}. The second criterion is met when the final force on any component of any atom does not exceed 10^{-12} eV/Å.

run

This command runs the molecular dynamics simulations for a specific number of timesteps. Simulations are run from between "100000000" and "200000000" (i.e. 100 to 200 million) timesteps, depending on pore size and simulation type. Simulations with higher molecular flux across the nanoporous graphene sheet are run for a smaller number of timesteps as simulation information is only required up to the first 20 or

so crossings, whereas simulations with lower molecular flux are run for the entire 200 million timesteps.

Chapter 5

Results

The effect of pore size on gas transport through nanoporous graphene membranes has been studied by generating a large number of molecular trajectories, and quantifying the molecular crossings that occur for graphene sheets with different pore sizes. The graphene sheet and gas species are modeled using the technique described in Chapter 3, while MD simulations are performed in LAMMPS using the architecture and numerical parameters discussed in Chapters 2 and 4 respectively. Sixteen replicates, each with a different random initial velocity seed, are performed for each pore size in order to minimize statistical uncertainty. Simulation outputs include a trajectory file that can be visualized in VMD (see figure 5-1) to reveal molecular phenomena of interest.

This chapter presents an analysis of the H_2/CH_4 and He/SF_6 simulation output, and calculates flow rates and permeabilities through the nanoporous graphene membrane. Pore sizes that enable the separation of the respective gas species are identified, and an optimal pore size is proposed for the separation of each pair of gases. Finally, the chapter concludes with a comparison of results obtained in the canonical (NVT) ensemble with those in the microcanonical (NVE) ensemble, to ensure that use of thermostats in simulation is justified and does not introduce any unphysical phenomena.

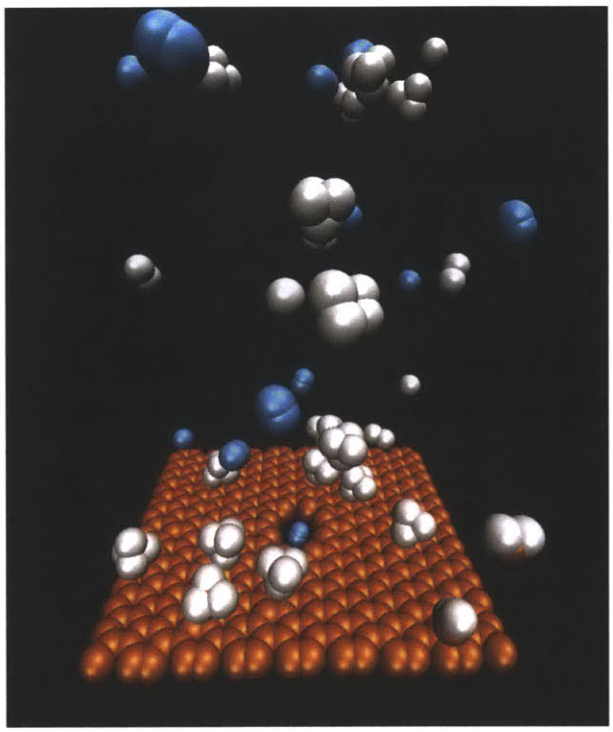

Figure 5-1: Illustration of a H_2 molecule (in blue) crossing the nanoporous graphene membrane (in orange). The pictured pore has a size of 10 lattice units, which is larger than the size of the H_2 molecule, allowing H_2 to cross with ease.

5.1 Identification of Pore Sizes for H_2/CH_4 Separation

The permeabilities of the graphene sheet to both H_2 and CH_4 are calculated using the approach described in Section 3.4 - converting the number of crossings into moles, then normalizing by the size of the graphene sheet, simulation duration and driving pressure difference. The permeabilities [mol/m^2 s Pa] are presented as a function of pore size in Table 5.1. In Table 5.1, the uncertainty associated with the permeability of a gas species for pore sizes with no observable crossings is estimated as the permeability for which there is a $> 95\%$ chance that a molecular crossing would have been observed in the total simulation duration of all 16 replicates (i.e. 640 ns). The estimated uncertainty, as derived from Poisson statistics, is a better approximation to the true uncertainty than the lack of any estimate. To put the computed permeability values

into context, the molar flow rate [mol/s] is calculated for a "industrial-sized" 10 cm $\times$ 10 cm graphene sheet with 1-4 % porosity, and a driving partial pressure difference of 1 atm. The molar flow rate is plotted as a function of pore size in Figure 5-2.

Table 5.1: Permeability of Nanoporous Graphene to H_2 and CH_4. The uncertainty associated with the permeability of a gas species for pore sizes with no observable crossings is estimated as the permeability for which there is a $>95\%$ chance that a molecular crossing would have been observed in the total simulation duration of all 16 replicates.

Pore Size (Units)	Porosity	H_2		CH_4	
		Permeability [mol/m^2 s Pa]	Std. Error [mol/m^2 s Pa]	Permeability [mol/m^2 s Pa]	Std. Error [mol/m^2 s Pa]
6	1.0 %	0	8.64×10^{-6}	0	8.64×10^{-6}
7	1.4 %	5.56×10^{-5}	1.44×10^{-5}	0	8.64×10^{-6}
10	2.4 %	1.09×10^{-3}	8.20×10^{-5}	0	8.64×10^{-6}
14	3.8 %	3.88×10^{-3}	4.33×10^{-4}	3.16×10^{-3}	3.67×10^{-4}

Figure 5-2 demonstrates that the permeability of nanoporous graphene is high for large pore sizes. As pore size is reduced, a greater decrease in permeability to CH_4 is observed, as compared to H_2. The differential transport rates of both species demonstrates the presence of a molecular size exclusion effect for a range of pore sizes. A pore size of 6 units or less is impermeable to H_2, whereas a pore size of 10 units or less is impermeable to CH_4. These results suggest that nanoporous graphene membranes with a pore size of 10 units are optimal for the separation of H_2 from CH_4. A high H_2 permeability can be achieved with excellent selectivity, as the pore is large enough to let H_2 pass with sufficiently large flux and small enough to be impermeable to CH_4.

The estimated permeability of H_2 through the graphene sheet with 2.4 % pore coverage, corresponding to one pore of size 10 units in a 9 nm^2 area, is approximately 1.1×10^{-3} mol/m^2 s Pa. This translates into a corrected molar flux of H_2 which is about 0.6 % that of the equilibrium flux on a surface in a dilute ideal gas. This is

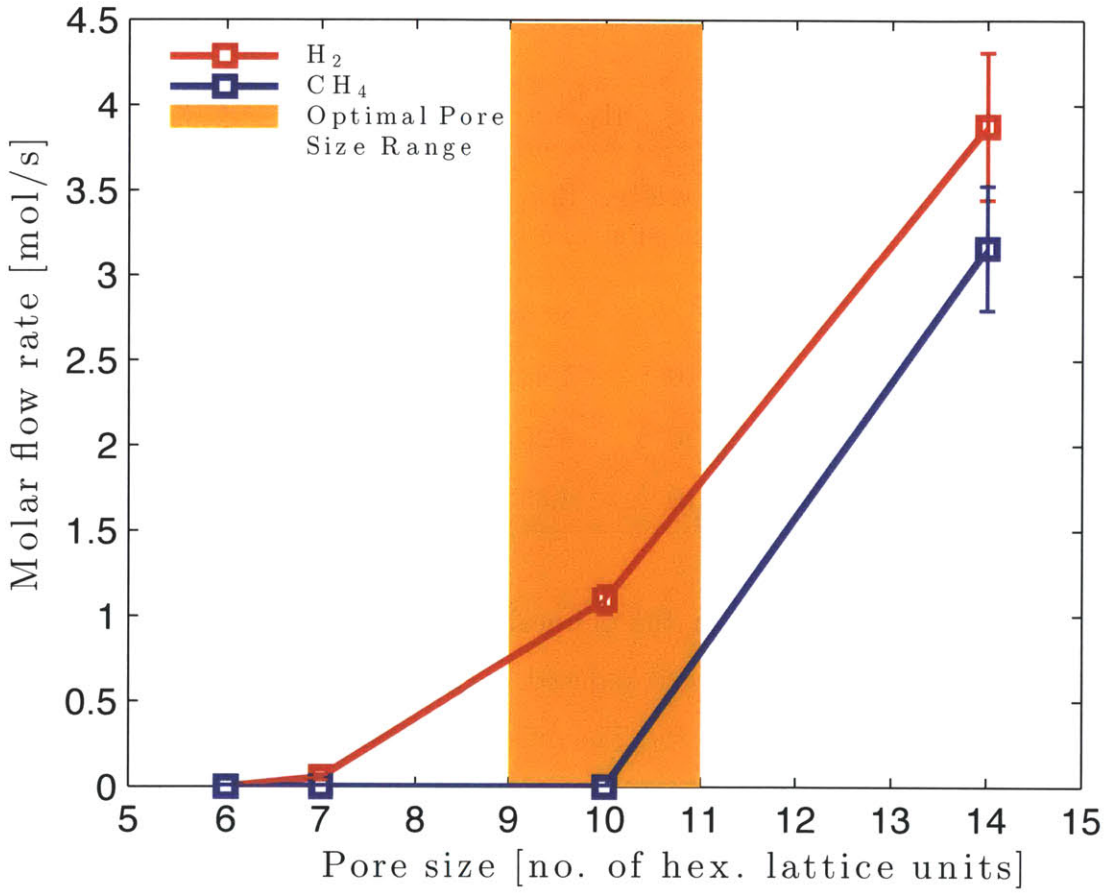

Figure 5-2: Molar flow rates of H_2 and CH_4 for different pore sizes across a $10\,cm^2$ graphene sheet, for a driving partial pressure difference of 1 atm.

more realistic than the predictions of Jiang et al. [24], for which the calculated flux is 5.5 times the equilibrium flux in an ideal gas.

The calculated permeability of H_2 is 3 to 4 orders of magnitude higher than existing state-of-the-art alumina membranes [3], which have permeabilities of about 5×10^{-7} mol/m^2 s Pa. Hence, graphene-based separation of H_2 from CH_4 has the potential to achieve permeabilities that are sufficiently high to be feasible for natural gas processing.

5.2 Identification of Pore Sizes for He/SF_6 Separation

The permeabilities of the graphene sheet to both He and SF_6 are calculated using the same approach as Section 5.1. The permeabilities [mol/m^2 s Pa] are presented as a function of pore size in Table 5.2. In Table 5.2, as with Table 5.1, the uncertainty associated with the permeability of a gas species for pore sizes with no observable crossings is estimated as the permeability for which there is a $>95\%$ chance that a molecular crossing would have been observed in the total simulation duration of all 16 replicates (i.e. 640 ns for 7 and 10 unit pores, 480 ns for 12 unit pore).

The molar flow rate [mol/s] is calculated for a "industrial-sized" 10 cm $\times$ 10 cm graphene sheet with porosity in the range 1-5 %, and a driving partial pressure difference of 1 atm, in analogy with the simulations described in the previous section. The molar flow rate is plotted as a function of pore size in Figure 5-3.

As observed for the H_2/CH_4 simulations, permeability is generally enhanced for both hydrogen and methane in membranes with larger pores. A molecular size exclusion effect is also present, as a greater decrease in permeability of SF_6 is observed as pore size is reduced. All pore sizes are permeable to He, whereas a pore size of 12 units or less is impermeable to SF_6. These results suggest that nanoporous graphene membranes with a pore size of 12 units are optimal for the separation of He from SF_6.

However, the calculated flow rate of SF_6 increases very slowly above 12 units,

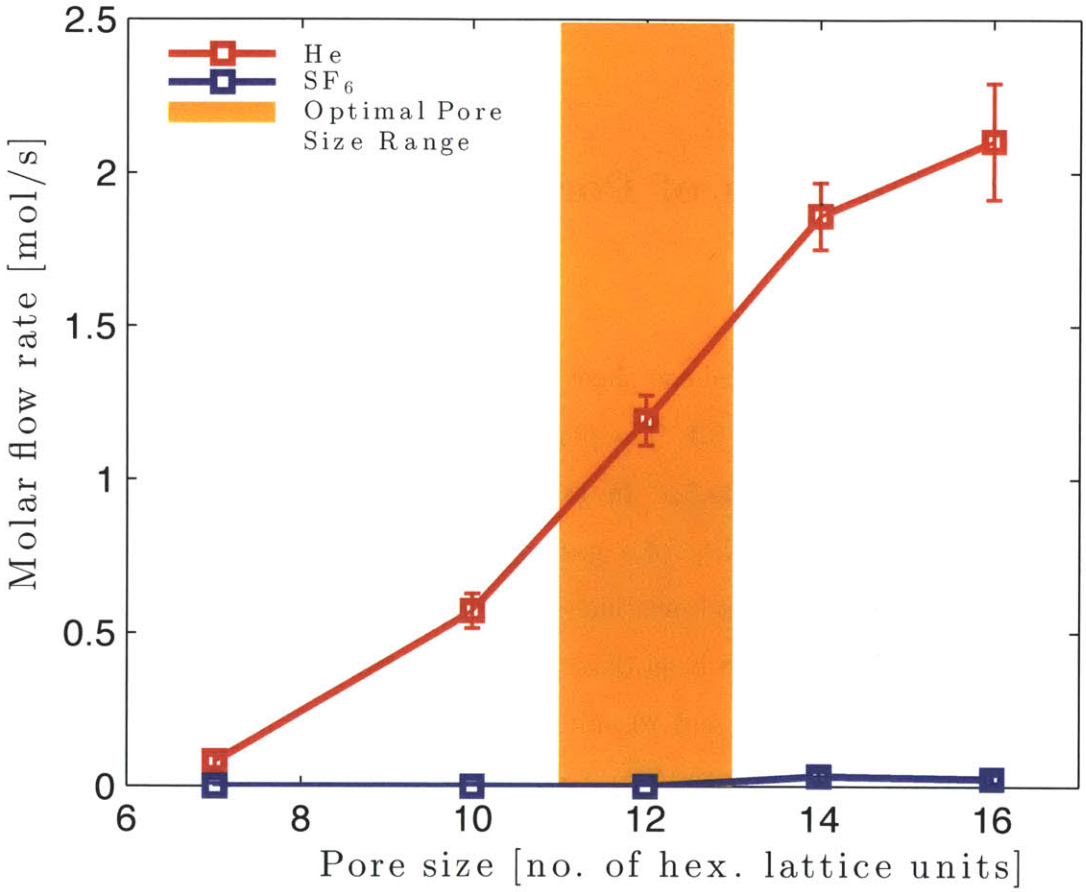

Figure 5-3: Molar flow rates of He and SF_6 for different pore sizes across a $10\,cm^2$ graphene sheet, for a driving partial pressure difference of 1 atm.

Table 5.2: Permeability of Nanoporous Graphene to He and SF_6. The uncertainty associated with the permeability of a gas species for pore sizes with no observable crossings is estimated as the permeability for which there is a $> 95\%$ chance that a molecular crossing would have been observed in the total simulation duration of all 16 replicates.

Pore Size (Units)	Porosity	He		SF_6	
		Permeability [mol/m^2 s Pa]	Std. Error [mol/m^2 s Pa]	Permeability [mol/m^2 s Pa]	Std. Error [mol/m^2 s Pa]
7	1.4 %	8.07×10^{-5}	1.93×10^{-5}	0	8.64×10^{-6}
10	2.4 %	5.71×10^{-4}	5.64×10^{-5}	0	8.64×10^{-6}
12	3.1 %	1.19×10^{-3}	8.19×10^{-5}	0	1.15×10^{-5}
14	3.8 %	1.86×10^{-3}	1.09×10^{-4}	3.33×10^{-5}	1.49×10^{-5}
16	4.6 %	2.10×10^{-3}	1.90×10^{-4}	2.53×10^{-5}	1.36×10^{-5}

and even decreases slightly between 14 and 16 units. This can be attributed to two different reasons. Firstly, as shown in Figure 3-2, the smallest dimension (i.e. critical dimension of approximately 5.0 Å) of the 14 unit and 16 unit pores is very similar, and also to the kinetic diameter of SF_6, (5.5 Å). The second reason pertains to the low frequency of SF_6 crossings and thus the (relatively) large statistical uncertainty in these measurements– a total of 4 and 7 crossings were recorded for all 16 simulations for the 14 and 16 unit pore respectively. However, of the 7 crossings observed throughout the simulation duration for the 16 unit pore, 4 of them occurred during the initial equilibration period of 6 ns and were disregarded. Only the remaining 3 crossings were used to calculate SF_6 flux. On the other hand, no crossings occurred during the initial equilibration period for the 14 unit pore, and the remaining 4 crossings gave rise to an SF_6 flux that exceeded the 16 unit pore.

The estimated permeability of He through the graphene sheet with 3.1 % pore coverage, corresponding to one pore of size 12 units in a 9 nm^2 area, is approximately 1.2×10^{-3} mol/m^2 s Pa. This translates into a corrected molar flux of He which is about 0.9 % that of the equilibrium flux on a surface in a dilute ideal gas, which is

realistic. Although there is no widely-known He/SF_6 industrial gas separation process against which the simulation data can be compared, these simulations were performed in an attempt to guide experimental studies of the same gases; due to the large size difference between the two molecules, this pair is likely to be one of the first to be experimentally tested.

5.3 Justification for Thermostat Usage

The results presented in the preceding sections were derived from simulations performed in the canonical (NVT) ensemble, through the application of a Nosé-Hoover chain thermostat. While thermostats are widely implemented to control the system temperature [28, 53, 54, 68], proof only exists that the Nosé-Hoover algorithm gives correct (canonical) dynamics for an equilibrium process. Since gas transport across nanoporous graphene membranes is a non-equilibrium process, no proof exists that the configurational degrees of freedom are distributed according to the correct non-equilibrium dynamics, although this is widely assumed to be true in the literature. Hence, ideally, simulation data should be collected in the NVE ensemble without the thermostat; this can be achieved by applying the thermostat during equilibration, but turning it off once the latter is completed. In this section, the temperature trajectories of non-thermostated simulations are investigated, to determine if non-thermostated simulations can be employed.

First, He/SF_6 simulations were performed on the 14 unit pore, by applying the thermostat for varying amounts of time during equilibration - 10×10^3, 20×10^6 and 50×10^6 timesteps. This was done to investigate whether temperature drifts occur once the thermostat is disabled. Figure 5-4 plots the temperature of the He/SF_6/graphene system after the thermostat is turned off, for all three equilibration durations.

When the thermostat is turned off after 10×10^3 equilibration steps and the simulation is run in the NVE ensemble, the temperature drifts downwards by 40 K, towards 260 K. On the other hand, the downward temperature drift is not observed when the thermostat is turned off after 20×10^6 equilibration steps or longer. During this time,

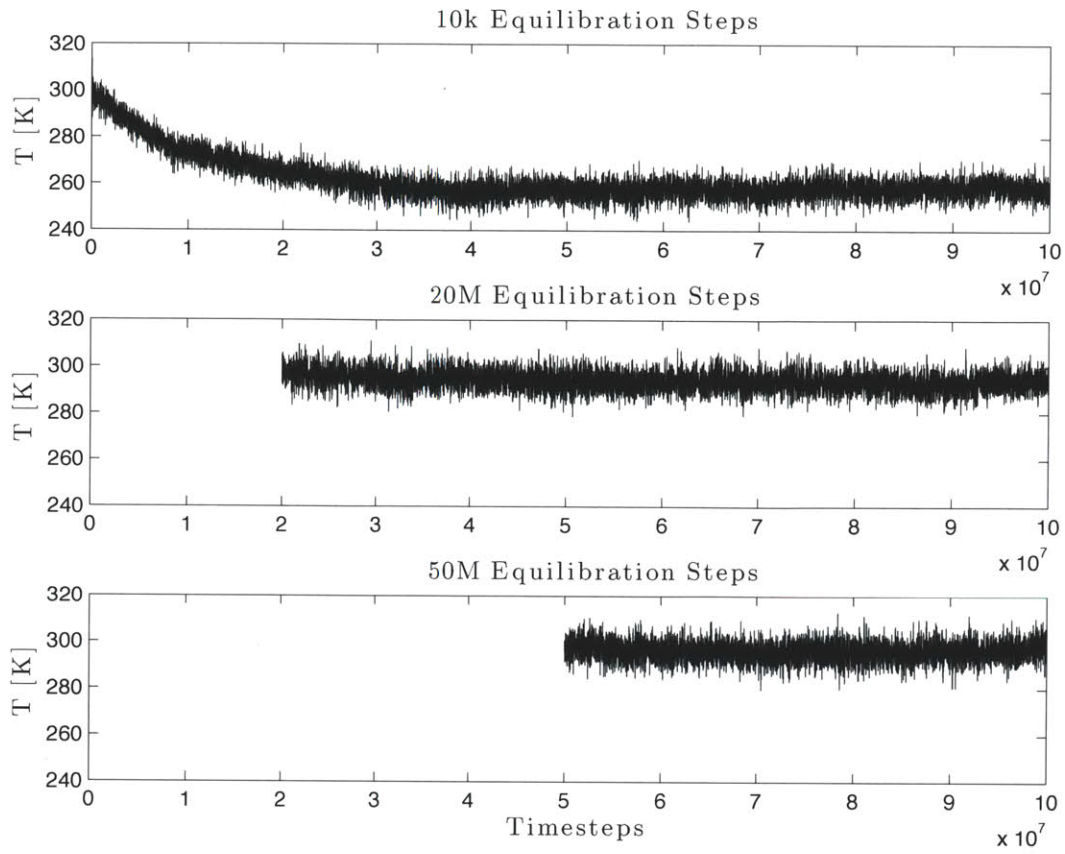

Figure 5-4: Temperature of He/SF_6 simulation after the thermostat is switched off. Equilibration was performed with the thermostat for varying amounts of time - 10×10^3, 20×10^6 and 50×10^6 timesteps. The temperature response for the thermostated duration is not shown.

the total simulation energy is approximately conserved. In other words, the change in temperature (kinetic energy) is due to energy redistribution between various modes available to the system. We attribute this energy redistribution to molecular collisions: a brief calculation reveals that the mean free time between collisions is on the order of 10×10^6 timesteps. In other words, this energy redistribution is a result of internal relaxation processes mediated by molecular collisions.

Our goal is to measure flow rates at 300 K without a thermostat, in order to verify that the results are not influenced by the thermostat. For this reason, we performed 16 simulations for the He/SF_6 system with a 14 unit pore, at an initial temperature of 340 K. In these simulations the thermostat is only applied for 10×10^3 equilibration

steps; subsequently, the temperature drifts from an initial value of 340 K to 300 K. The average temperature of the 16 replicates is plotted in Figure 5-5.

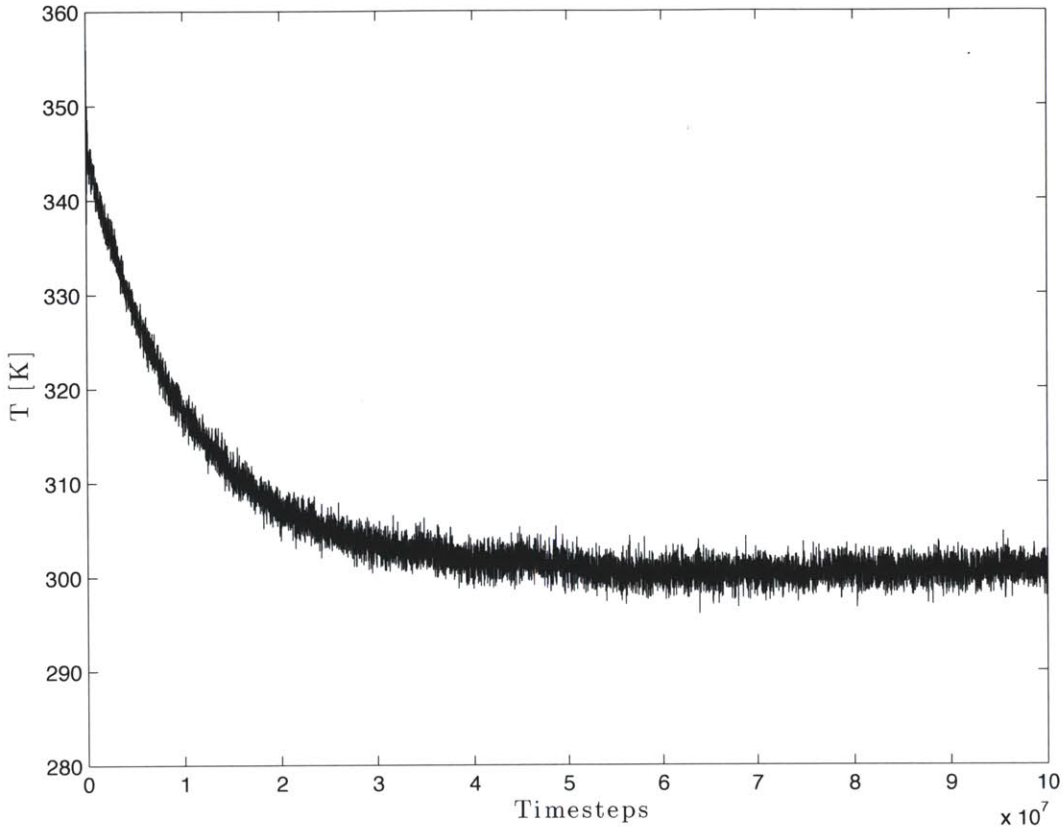

Figure 5-5: Average temperature of 16 replicates for the He/SF_6 simulation with a 14 unit pore, and 10×10^3 equilibration steps. The temperature is initialized at 340 K to allow it to drift downwards and equilibrate to the target temperature of 300 K.

Figure 5-5 verifies that these simulations have equilibrated at a temperature of approximately 300 K without a thermostat and can thus be used to validate the thermostated simulation results discussed in Section 5.2. The average permeability of the graphene sheet to He is found to be $1.55 \pm 0.136\times10^{-3}$ mol/m^2 s Pa. This value is about 17 % smaller than the simulations performed in the NVT ensemble, which yield a permeability of $1.86 \pm 0.109\times10^{-3}$ mol/m^2 s Pa. The discrepancy of 17 % is larger than the 6 % standard error associated with the calculated permeability in the NVT ensemble, and also exceeds the combined uncertainties of the two measurements. The average permeability of the graphene sheet to SF_6 is calculated to

be $0 \pm 1.73 \times 10^{-5}$ mol/m^2 s Pa, as compared to $3.33 \pm 1.49 \times 10^{-5}$ mol/m^2 s Pa for the thermostated simulations. While the discrepancy is slightly larger than the 45 % standard error associated with the calculated permeability in the NVT ensemble, it is possible that the discrepancy is caused by the very low frequency of SF_6 crossings. A total of 3 crossings were recorded for all 16 NVE simulations for the 14 unit pore. However, all 3 crossings occurred during the first 30×10^6 timesteps, an equilibration period, thus none of the crossings contributed to the calculated SF_6 flux. On the other hand, a total of 4 crossings were recorded for all 16 thermostated simulations for the 14 unit pore, with no crossings during the equilibration period. In summary, the NVE and NVT simulations yield results that differ by an amount that is slightly greater than the statistical uncertainty of the simulations. However, additional factors, such as the flux correction described in Section 3.4 (equation 3.2) may have contributed to this discrepancy. Overall, the differences between the NVE and NVT simulations are very close to being within the statistical uncertainty of the simulations, suggesting that the dynamics simulated by the Nosé-Hoover thermostat are reasonably realistic.

H_2/CH_4 simulations with a 10 unit pore are performed in the NVE ensemble in an analogous way to the He/SF_6 simulations, turning off the thermostat after 10×10^3 timesteps and initializing the temperature at 320 K (a 20 K downward temperature drift to a local minimum is observed at the initial phases of the NVE simulation, but this adjustment is unnecessary as the temperature subsequently diverges upwards). The average temperature of the 16 replicates is plotted in Figure 5-6 for the H_2/CH_4 NVE simulations.

The temperature diverges upwards after approximately 20×10^6 timesteps, and does not reach an equilibrium value. The temperature divergence can be attributed to the poor energy conservation observed in the NVE simulations for the H_2/CH_4/graphene system with interactions described by the AIREBO potential, even though the same timestep of 0.2 fs is employed. To verify this assertion, the timestep was reduced by a factor of 3 to 0.067 fs and simulations otherwise identical to those presented in Figure 5-6 are performed in the NVE ensemble. The average temperature history of 4 such replicates is plotted in Figure 5-7.

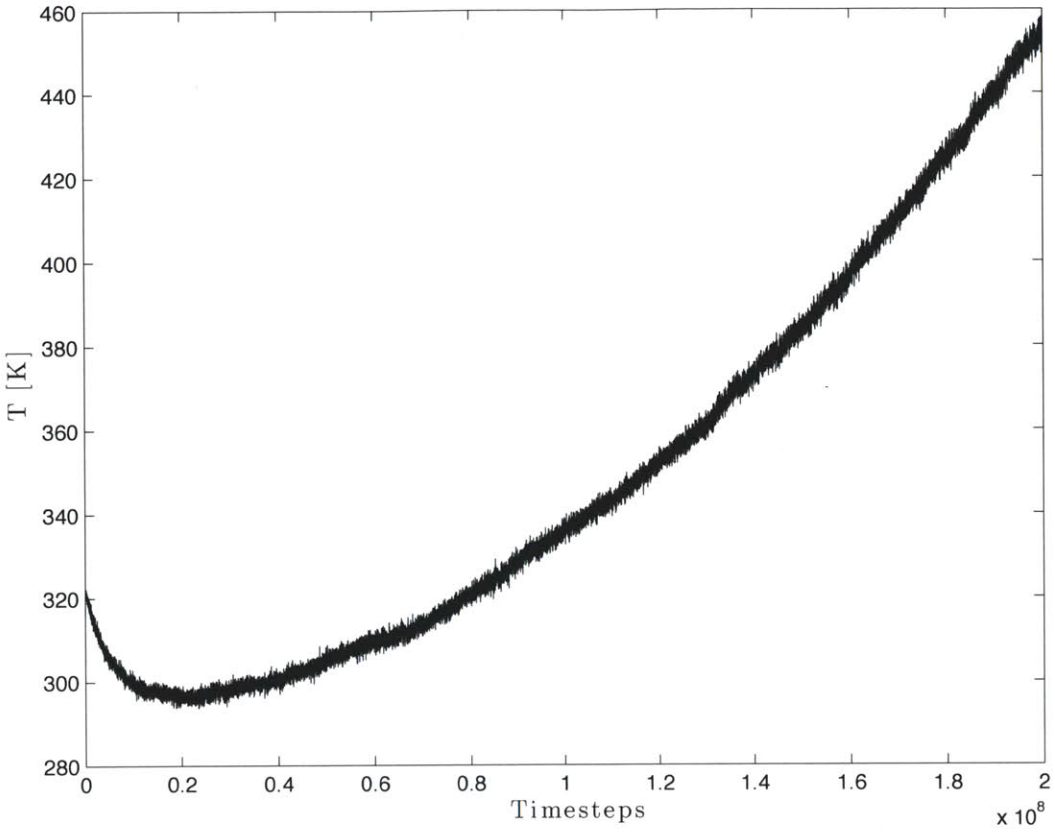

Figure 5-6: Average temperature of 16 replicates for the H_2/CH_4 simulation with a 10 unit pore, and 10×10^3 equilibration steps. The temperature is initialized at 320 K, but attains a local minimum at 300 K and diverges upwards.

Figure 5-7 shows that the simulations with the smaller timestep have equilibrated at a temperature of about 293 K. In these simulations, energy is conserved, indicating that the previously chosen timestep of 0.2 fs may be too large. However, due to the computational expense associated with the reduced timestep, we have not been able to perform a direct comparison of the NVE and NVT results of the same process as in the case of the He/SF_6 system.

5.3.1 Conclusions on Thermostat Usage

This section demonstrates that turning off the Nosé-Hoover thermostat to perform simulations in the NVE ensemble results in a temperature drift, and suggests that the temperature drift could be due to long-time equilibration of the molecules or lack

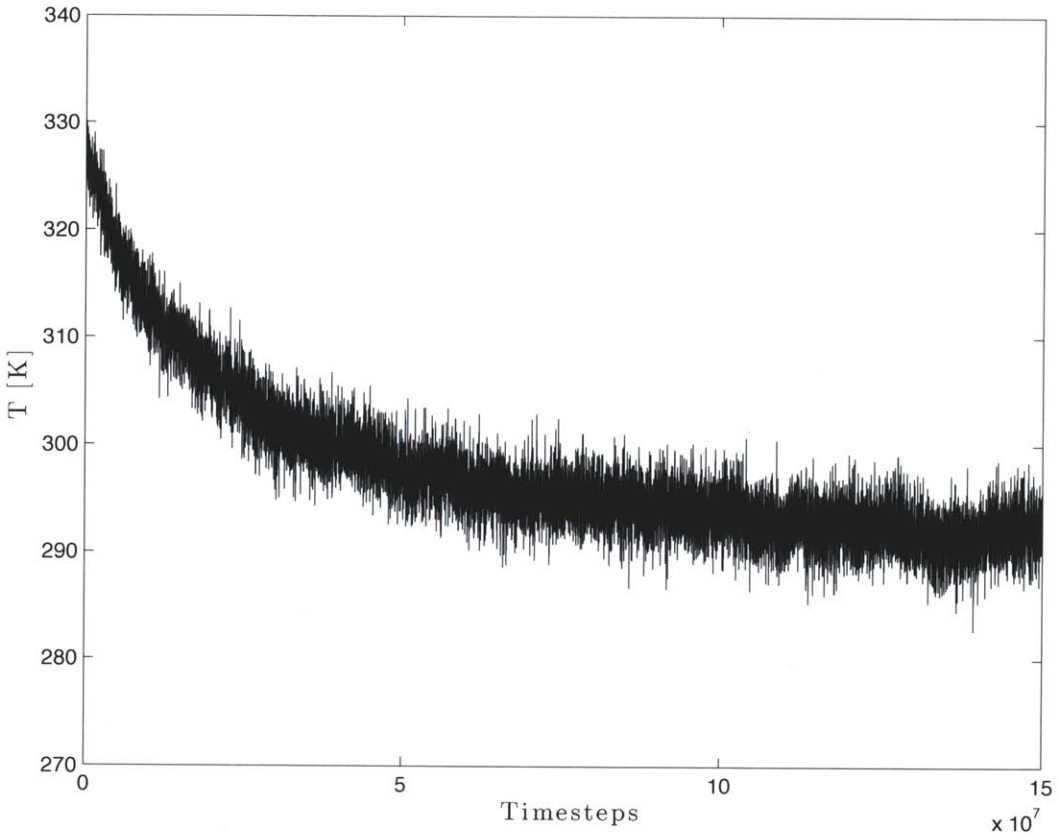

Figure 5-7: Average temperature of 4 replicates for the H_2/CH_4 simulation with a 10 unit pore, 10×10^3 equilibration steps, and a reduced timestep of 0.067 fs. The temperature is initialized at 320 K, but drifts downwards and equilibrates to a temperature of 293 K.

of energy conservation. NVE results can be compared to thermostated results if the temperature drifts towards a steady-state value, by choosing an appropriate initial temperature, as performed for the He/SF_6 simulations. The length of time taken for the He/SF_6 NVE simulations to equilibrate is approximately 30×10^6 timesteps or 6 ns, validating the choice of duration of the equilibration phase in thermostated simulations. We have been unable to obtain a steady state temperature in non-thermostated H_2/CH_4 simulations for the timestep of 0.2 fs (which is employed in NVT simulations), as energy is not conserved. However, a reduced timestep of 0.067 fs yields a steady state temperature with energy conservation, suggesting that the previously chosen timestep of 0.2 fs may be too large. However, due to the computational expense of the reduced timestep H_2/CH_4 simulations, only simulations with the Nosé-Hoover

thermostat and a timestep of 0.2 fs are presented in this thesis.

Chapter 6

Summary and Future Work

We have performed a theoretical, molecular dynamics-based study to elucidate the effect of pore size on gas transport across nanoporous graphene membranes. This is the first step towards realizing the first nanoporous graphene membrane for gas separation, which is expected to yield high selectivity and permeability due to the unique properties of graphene.

We modeled the separation of gas components from a mixture using a graphene sheet with engineered pores of different sizes. We subsequently employed molecular dynamics simulations to calculate a large number of molecular trajectories, in order to obtain low-statistical-uncertainty estimates of transport rates through the graphene membrane using the initial flux approximation. Simulations were performed on two different gas mixtures - a helium-sulfur hexafluoride mixture, for which the large difference in molecular size lends itself to a size-based separation approach, and a hydrogen-methane mixture, which is relevant to natural gas processing. The AIREBO potential was used to describe both covalent and long-range intermolecular interactions in the hydrogen-methane-graphene system, while a more versatile hybrid potential formulation was chosen for the helium-sulfur hexafluoride-graphene system. We have found that for a timestep of 0.2 fs, energy is not conserved in the hydrogen-methane-graphene system, necessitating a significantly smaller timestep that was beyond the capability of our computational resources. A study of this system in the NVE ensemble at this smaller timestep should be undertaken in order to validate the

results of Section 5.1.

Our simulations demonstrate the presence of a molecular size exclusion effect for a range of pore sizes. This enables a pore size to be determined that achieves high selectivity in gas separation, while exhibiting high permeability for the desired gas species. The calculated molar flux of hydrogen is shown to be more realistic than the predictions made in previous work. In addition, the calculated permeability of hydrogen through the graphene sheet is shown to be orders of magnitude higher than existing state-of-the-art alumina membranes, and is sufficiently high to be commercially viable for natural gas processing applications.

Future work should include an investigation of the effects of pore geometry and functionalization with terminal groups, further guiding the development of nanoporous graphene membranes. This will become increasingly important when techniques that provide precise control over nanopore size and characteristics are developed. Simulations can also be performed to elucidate the role of imperfections such as membrane defects and variability in pore distribution, as a topic of both practical and theoretical significance. The results of this work and subsequent work on nanopore modeling can be extended to calculate transmission probabilities of various gas species, to be used in coarse-grained models of the gas separation devices of the future.

Bibliography

[1] L. M. Robeson. Correlation of separation factor versus permeability for polymeric membranes. *Journal of Membrane Science*, 62(2):165–185, 1991.

[2] S. J. Stuart, A. B. Tutein, and J. A. Harrison. A reactive potential for hydrocarbons with intermolecular interactions. *Journal of Chemical Physics*, 112(14):6472–6486, 2000.

[3] S. Adhikari and S. Fernando. Hydrogen Membrane Separation Techniques. *Industrial & Engineering Chemistry Research*, 45(3):875–881, 2006.

[4] E. S. Kikkinides, R. T. Yang, and S. H. Cho. Concentration and Recovery of CO_2 from Flue Gas by Pressure Swing Adsorption. *Industrial & Engineering Chemistry Research*, 32(11):2714–2720, 1993.

[5] G. Q. Miller and J. Stoecker. *Selection of a hydrogen separation process.* National Petroleum Refiners Association, Washington, DC, 1989.

[6] A. B. Hinchliffe and K. E. Porter. A Comparison of Membrace Separation and Distillation. *Chemical Engineering Research and Design*, 78(2):255–268, 2000.

[7] S. Sircar and T. C. Golden. Purification of Hydrogen by Pressure Swing Adsorption. *Separation Science & Technology*, 35(5):667–687, 2000.

[8] S. C. A. Kluiters. Status review on membrane systems for hydrogen separation. Technical Report ECN–C—04–102, 5^{th} Research Framework Programme of the European Union, December 2004.

[9] W. J. Koros and G. K. Fleming. Membrane-based gas separation. *Journal of Membrane Science*, 83(1):1–80, 1993.

[10] D. R. Paul and Y. P. (ed.) Yampol'skii. *Polymeric Gas Separation Membranes.* CRC Press Inc., Boca Raton, 1994.

[11] H. Chen. *Atomic Simulations of Gas Mixture Separation through Nanoporous Membraces.* PhD thesis, Carnegie Mellon University, Pittsburgh, Pennsylvania, 2007.

[12] R. W. Baker. Future Directions of Membrane Gas Separation Technology. *Industrial & Engineering Chemistry Research*, 41(6):1393–1411, 2002.

[13] R. W. Baker. *Membrane Technology and Applications.* Wiley, Chichester, U.K., 2nd edition, 2004.

[14] P. Bernardo, E. Drioli, and G. Golemme. Membrane Gas Separation: A Review/State of the Art. *Industrial & Engineering Chemistry Research*, 48(10):4638–4663, 2009.

[15] D. M. D'Alessandro, B. Smit, and J. R. Long. Carbon Dioxide Capture: Prospects for New Materials. *Angewandte Chemie*, 49(35):6058–6082, 2010.

[16] R. W. Baker. Research needs in the membrane separation industry: Looking back, looking forward. *Journal of Membrane Science*, 362(1-2):134–136, 2010.

[17] R. W. Baker and K. Lokhandwala. Natural Gas Processing with Membranes: An Overview. *Industrial & Engineering Chemistry Research*, 47(7):2109–2121, 2008.

[18] M. J. Allen, V. C. Tung, and R. B. Kaner. Honeycomb Carbon: A Review of Graphene. *Chemical Reviews*, 110(1):132–145, 2010.

[19] A. K. Geim. Graphene: Status and Prospects. *Science*, 324(5394):1530–1534, 2009.

[20] C. Lee, X. Wei, J. W. Kysar, and J. Hone. Measurement of the Elastic Properties and Intrinsic Strength of Monolayer Graphene. *Science*, 321(5887):385–388, 2008.

[21] Z. S. Wu, W. Ren, L. Gao, J. Zhao, Z. Chen, B. Liu, D. Tang, B. Yu, C. Jiang, and H. M. Cheng. Synthesis of Graphene Sheets with Huge Electrical Conductivity and Good Thermal Stability by Hydrogen Arc Discharge Exfoliation. *ACS Nano*, 3(2):411–417, 2009.

[22] J. S. Bunch, S. S. Verbridge, J. S. Alden, A. M. van der Zande, J. M. Parpia, H. G. Craighead, and P. L. McEuen. Impermeable Atomic Membranes from Graphene Sheets. *Nano Letters*, 8(8):2458–2462, 2008.

[23] S. Blankenburg, M. Bieri, R. Fasel, K. Mullen, C. A. Pignedoli, and D. Passerone. Porous Graphene as an Atmospheric Nanofilter. *Small*, 6(20):2266–2271, 2010.

[24] D. E. Jiang, V. R. Cooper, and S. Dai. Porous graphene as the ultimate membrane for gas separation. *Nano Letters*, 9(12):4019–4024, 2009.

[25] O. Leenaerts, B. Partoens, and F. M. Peeters. Graphene: A perfect nanoballoon. *Applied Physics Letters*, 93(19):193107, 2008.

[26] J. Schrier. Helium Separation Using Porous Graphene Membranes. *The Journal of Physical Chemistry Letters*, 1:2284–2287, 2010.

[27] K. Sint, B. Wang, and P. Král. Selective Ion Passage through Functionalized Graphene Nanopores. *Journal of the American Chemical Society*, 130(49):16448–16449, 2008.

[28] M. E. Suk and N. R. Aluru. Water Transport through Ultrathin Graphene. *Journal of Physical Chemistry Letters*, 1(10):1590–1594, 2010.

[29] K. S. Novoselov, A. K. Geim, S. V. Morozov, D. Jiang, Y. Zhang, S. V. Dubonos, I. V. Grigorieva, and A. A. Firsov. Electric Field Effect in Atomically Thin Carbon Films. *Science*, 306(5696):666–669, 2004.

[30] X. Li, W. Cai, J. An, S. Kim, J. Nah, D. Yang, R. Piner, A. Velamakanni, I. Jung, E. Tutuc, S. K. Banerjee, L. Colombo, and R. S. Ruoff. Large-Area Synthesis of High-Quality and Uniform Graphene Films on Copper Foils. *Science*, 324(5932):1312–1314, 2009.

[31] A. Reina, X. Jia, J. Ho, D. Nezich, H. Son, V. Bulovic, M. S. Dresselhaus, and J. Kong. Large Area, Few-Layer Graphene Films on Arbitrary Substrates by Chemical Vapor Deposition. *Nano Letters*, 9(1):30–35, 2009.

[32] S. Bae, H. Kim, Y. Lee, X. Xu, J. S. Park, Y. Zheng, J. Balakrishnan, T. Lei, H. R. Kim, Y. I. Song, Y. J. Kim, K. S. Kim, B. Özyilmaz, J. H. Ahn, B. H. Hong, and S. Iijima. Roll-to-roll production of 30-inch graphene films for transparent electrodes. *Nature Nanotechnology*, 5:574–578, 2010.

[33] J. Zhang, H. Zou, Q. Qing, Y. Yang, Q. Li, Z. Liu, X. Guo, and Z. Du. Effect of Chemical Oxidation on the Structure of Single-Walled Carbon Nanotubes. *The Journal of Physical Chemistry B*, 107(16):3712–3718, 2003.

[34] I. Inui, K. Mochiji, K. Moritani, and N. Nakashima. Molecular dynamics simulations of nanopore processing in a graphene sheet by using gas cluster ion beam. *Applied Physics A: Materials Science & Processing*, 98(4):787–794, 2010.

[35] A. V. Krasheninnikov, K. Nordlund, and J. Keinonen. Production of defects in supported carbon nanotubes under ion irradiation. *Physical Review B*, 65(16):165423, 2002.

[36] A. V. Krasheninnikov, K. Nordlund, M. Sirviö, E. Salonen, and J. Keinonen. Formation of ion-irradiation-induced atomic-scale defects on walls of carbon nanotubes. *Physical Review B*, 63(24):245405, 2001.

[37] M. M. Lucchese, F. Stavale, E. H. M. Ferreira, C. Vilani, M. V. O. Moutinho, R. B. Capaz, C. A. Achete, and A. Jorio. Quantifying ion-induced defects and Raman relaxation length in graphene. *Carbon*, 48(5):1592–1597, 2010.

[38] J. A. V. Pomoell, A. V. Krasheninnikov, K. Nordlund, and J. Keinonen. Ion ranges and irradiation-induced defects in multiwalled carbon nanotubes. *Journal of Applied Physics*, 96(5):2864–2871, 2004.

[39] M. D. Fischbein and M. Drndić. Electron Beam Nanosculpting of Suspended Graphene Sheets. *Applied Physics Letters*, 93(11):113107, 2008.

[40] A. Hashimoto, K. Suenaga, A. Gloter, K. Urita, and S. Iijima. Direct evidence for atomic defects in graphene layers. *Nature*, 430(7002):870–873, 2004.

[41] J. P. Perdew, K. Burke, and M. Ernzerhof. Generalized Gradient Approximation Made Simple. *Physical Review Letters*, 77(18):3865–3868, 1996.

[42] M. Dion, H. Rydberg, E. Schröder, D. C. Langreth, and B. I. Lundqvist. Van der Waals Density Functional for General Geometries. *Physical Review Letters*, 92(24):246401, 2004.

[43] T. Thonhauser, V. R. Cooper, S. Li, A. Puzder, P. Hyldgaard, and D. C. Langreth. Van der Waals density functional: Self-consistent potential and the nature of the van der Waals bond. *Physical Review B*, 76(12):125112, 2007.

[44] R. M. de Vos and H. Verweij. High-Selectivity, High-Flux Silica Membranes for Gas Separation. *Science*, 279(5357):1710–1711, 1998.

[45] D. M. Ford and E. D. Glandt. Molecular Simulation Study of the Surface Barrier Effect. Dilute Gas Limit. *The Journal of Physical Chemistry*, 99(29):11543–11549, 1995.

[46] B. Ibeh, C. Gardner, and M. Ternan. Separation of hydrogen from a hydrogen/methane mixture using a PEM fuel cell. *International Journal of Hydrogen Energy*, 32(7):908–914, 2007.

[47] D. Hofman, J. Ulbrich, D. Fritsch, and D. Paul. Molecular modeling simulation of gas transport in amorphous polyimide and poly(amide imide) membrane materials. *Polymer*, 37(21):4773–4785, 1996.

[48] N. A. Seaton, S. P. Friedman, J. M. D. MacElroy, and B. J. Murphy. The Molecular Sieving Mechanism in Carbon Molecular Sieves: A Molecular Dynamics and Critical Path Analysis. *Langmuir*, 13(5):1199–1204, 1997.

[49] L. Xu, M. G. Sedigh, M. Sahimi, and T. T. Tsotsis. Nonequilibrium Molecular Dynamics Simulation of Transport of Gas mixtures in Nanopores. *Physical Review Letters*, 80(16):3511–3514, 1998.

[50] L. Xu, T. T. Tsotsis, and M. Sahimi. Nonequilibrium molecular dynamics simulation of transport and separation of gases in carbon nanopores. I. Basic results. *Journal of Chemical Physics*, 111(7):3252–3264, 1999.

[51] L. Xu, M. G. Sedigh, T. T. Tsotsis, and M. Sahimi. Nonequilibrium molecular dynamics simulation of transport and separation of gases in carbon nanopores. II. Binary and ternary mixtures and comparison with the experimental data. *Journal of Chemical Physics*, 112(2):910–922, 2000.

[52] L. Xu, M. Sahimi, and T. T. Tsotsis. Nonequilibrium molecular dynamics simulation of transport and separation of gas mixtures in nanoporous materials. *Physical Review E*, 62(5):6942–6948, 2000.

[53] D. Sen, K. S. Novoselov, P. M. Reis, and M. J. Buehler. Tearing Graphene Sheets From Adhesive Substrates Produces Tapered Nanoribbons. *Small*, 6(10):1108–1116, 2010.

[54] D. Cohen-Tanugi and J. C. Grossman. Water Desalination across Nanoporous Graphene. *Nano Letters*, 2012.

[55] M. J. Buehler. *Atomistic Modeling of Materials Failure*. Springer, New York ; London, 2008.

[56] S. Plimpton. Fast Parallel Algorithms for Short-Range Molecular Dynamics. *Journal of Computational Physics*, 117:1–19, 1995.

[57] W. Humphrey, A. Dalke, and K. Schulten. VMD: Visual Molecular Dynamics. *Journal of Molecular Graphics*, 14:33–38, 1996.

[58] A. Rahman. Correlations in the Motion of Atoms in Liquid Argon. *Physical Review*, 136(2A):A405–A411, 1964.

[59] R. Komanduri, N. Chandrasekaran, and L. M. Raff. Molecular dynamics (MD) simulation of uniaxial tension of some single-crystal cubic metals at nanolevel. *International Journal of Mechanical Sciences*, 43(10):2237–2260, 2001.

[60] M. W. Finnis and J. E. Sinclair. A simple empirical N-body potential for transition metals. *Philosophical Magazine A*, 50(1):45–55, 1984.

[61] A. D. MacKerell, D. Bashford, M. Bellott, R. L. Dunbrack, J. D. Evanseck, M. J. Field, S. Fischer, J. Gao, H. Guo, S. Ha, D. Joseph-McCarthy, L. Kuchnir, K. Kuczera, F. T. K. Lau, C. Mattos, S. Michnick, T. Ngo, D. T. Nguyen, B. Prodhom, W. E. Reiher, B. Roux, M. Schlenkrich, J. C. Smith, R. Stote, J. Straub, M. Watanabe, J. Wiórkiewicz-Kuczera, D. Yin, and M. Karplus. All-Atom Empirical Potential for Molecular Modeling and Dynamics Studies of Proteins. *The Journal of Physical Chemistry B*, 102(18):3586–3616, 1998.

[62] J. Tersoff. New empirical model for the structural properties of silicon. *Physical Review Letters*, 56(6):632–635, 1986.

[63] D. W. Brenner. Empirical potential for hydrocarbons for use in simulating the chemical vapor deposition of diamond films. *Physical Review B*, 42(15):9458–9471, 1990.

[64] D. W. Brenner, O. A. Shenderova, J. A. Harrison, S. J. Stuart, B. Ni, and S. B. Sinnott. A second-generation reactive empirical bond order (REBO) potential energy expression for hydrocarbons. *Journal of Physics Condensed Matter*, 14(4):783–802, 2002.

[65] A. C. T. van Duin, S. Dasgupta, F. Lorant, and W. A. Goddard. ReaxFF: A Reactive Force Field for Hydrocarbons. *The Journal of Physical Chemistry A*, 105(41):9396–9409, 2001.

[66] J. Schrier. Carbon Dioxide Separation with a Two-dimensional Polymer Membrane. *ACS Applied Materials & Interfaces*, 2012.

[67] Z. Xu and M. J. Buehler. Nanoengineering Heat Transfer Performance at Carbon Nanotube Interfaces. *ACS Nano*, 3(9):2767–2775, 2009.

[68] H. Zhao, K. Min, and N. R. Aluru. Size and Chirality Dependent Elastic Properties of Graphene Nanoribbons under Uniaxial Tension. *Nano Letters*, 9(8):3012–3015, 2009.

[69] M. P. Allen and D. J. Tildesley. *Computer Simulation of Liquids.* Oxford, New York, 1989.

[70] D. Dellis and J. Samios. Molecular force field investigation for Sulfur Hexafluoride: A computer simulation study. *Fluid Phase Equilibria*, 291(1):81–89, 2010.

[71] R. B. Ross and S. S. Mohanty. *Multiscale Simulation Methods for Nanomaterials.* Wiley, Hoboken, New Jersey, 2008.

[72] Y. S. Lin and M. Kanezashi. Gas permeation and diffusion in small and intermediate pore zeolite membranes. *Studies in Surface Science and Catalysis*, 170:847–854, 2007.

[73] Ç. Ö. Girit, J. C. Meyer, R. Erni, M. D. Rossell, C. Kisielowski, L. Yang, C. H. Park, M. F. Crommie, M. L. Cohen, S. G. Louie, and A. Zettl. Graphene at the Edge: Stability and Dynamics. *Science*, 323(5922):1705–1708, 2009.

[74] J. Stone. An Efficient Library for Parallel Ray Tracing and Animation. Master's thesis, Computer Science Department, University of Missouri-Rolla, April 1998.

[75] W. G. Hoover. Canonical dynamics: Equilibrium phase-space distributions. *Physical Review A*, 31(3):1695–1697, 1985.

[76] S. Nosé. A unified formulation of the constant temperature molecular dynamics methods. *Journal of Chemical Physics*, 81(1):511–519, 1984.

[77] J. P. Ryckaert, G. Ciccotti, and H. J. C. Berendsen. Numerical integration of the cartesian equations of motion of a system with constraints: molecular dynamics of n-alkanes. *Journal of Computational Physics*, 23(3):327–341, 1977.

[78] W. Shinoda, M. Shiga, and M. Mikami. Rapid estimation of elastic constants by molecular dynamics simulation under constant stress. *Physical Review B*, 69(13):134103, 2004.